Saadi *et al. Microstructures* **2025**, *5*, 2025092
DOI: 10.20517/microstructures.2024.136

Microstructures

Review

Open Access

Exploring the underlying mechanisms of ferroelectric behavior in metal-doped aluminum nitride: an in-depth review

Mohamed Saadi[1,2], Weijing Shao[3,4], Miaocheng Zhang[1,5], Haiming Qin[1,6], Cong Han[1,6], Youde Hu[1], Hao Zhang[1], Xinpeng Wang[1], Yi Tong[1,7]

[1]Gusu Laboratory of Materials, Suzhou 215123, Jiangsu, China.
[2]Laboratoire LMOP, Université de Tunis El Manar, Tunis 2092, Tunisia.
[3]Suzhou Laboratory, Suzhou 215123, Jiangsu, China.
[4]Faculty of Integrated Circuit, Xidian University, Xi'an 710071, Shaanxi, China.
[5]College of Electronic and Optical Engineering & College of Flexible Electronics (Future Technology), Nanjing University of Posts and Telecommunications, Nanjing 210023, Jiangsu, China.
[6]College of Integrated Circuit Science and Engineering, Nanjing University of Posts and Telecommunications, Nanjing 210023, Jiangsu, China.
[7]The Institute of Semiconductors, Chinese Academy of Sciences, Beijing 100083, China.

Correspondence to: Dr. Mohamed Saadi, Gusu Laboratory of Materials, 388 Ruoshui Road, Suzhou 215123, Jiangsu, China. E-mail: saadi-mohamed@live.fr; Prof. Yi Tong, Gusu Laboratory of Materials, 388 Ruoshui Road, Suzhou 215123, Jiangsu, China. E-mail: tongyi2020@gusulab.ac.cn

How to cite this article: Saadi, M.; Shao, W.; Zhang, M.; Qin, H.; Han, C.; Hu, Y.; Zhang, H.; Wang, X.; Tong, Y. Exploring the underlying mechanisms of ferroelectric behavior in metal-doped aluminum nitride: an in-depth review. *Microstructures* **2025**, *5*, 2025092. https://dx.doi.org/10.20517/microstructures.2024.136

Received: 27 Nov 2024 **First Decision:** 28 Mar 2025 **Revised:** 6 Jun 2025 **Accepted:** 16 Jul 2025 **Published:** 11 Sep 2025

Academic Editor: Zuhuang Chen **Copy Editor:** Fangling Lan **Production Editor:** Fangling Lan

Abstract

This review explores the intricate relationship between metal doping and the polarization-switching dynamics of wurtzite-phase aluminum nitride (AlN) thin films. We examine how the dopant type, concentration, and resulting crystal structure affect the ferroelectric characteristics of AlN. Particular emphasis is placed on scandium-doped AlN (AlScN), a leading candidate for next-generation ferroelectric applications. We investigate the fundamental mechanisms underlying polarization switching, emphasizing the roles of local chemical interactions, structural modifications, and domain wall dynamics. In addition, we present a comparative analysis of key synthesis techniques - including magnetron sputtering, molecular beam epitaxy, atomic layer deposition, and pulsed laser deposition - highlighting their respective advantages and limitations in fabricating high-quality ferroelectric films. By elucidating the core principles governing ferroelectricity in doped AlN, this review provides valuable insights for

the design and optimization of advanced ferroelectric devices aimed at improving performance and energy efficiency.

Keywords: Ferroelectricity, AlScN, AlN, wurtzite, materials science

INTRODUCTION

Ferroelectric materials, characterized by electrically switchable spontaneous polarization, are integral to the advancement of modern technologies such as non-volatile memories, energy-efficient electronics, sensors, and neuromorphic computing systems. However, conventional perovskite ferroelectrics (e.g., $PbZr_xTi_{1-x}O_3$) face significant challenges, including limited compatibility with complementary metal-oxide-semiconductor (CMOS) processes, environmental concerns due to lead content, and degradation at elevated temperatures. These limitations have spurred the search for alternative ferroelectrics that offer strong performance, scalable fabrication, and seamless integration with existing semiconductor platforms.

Among emerging alternatives, aluminum nitride (AlN), a III-nitride semiconductor with a wide bandgap (~6.2 eV), has garnered attention due to its exceptional properties, including high thermal conductivity, excellent chemical stability, notable piezoelectric and pyroelectric responses, and compatibility with silicon-based technologies. AlN crystallizes in the wurtzite structure, a non-centrosymmetric lattice that generates strong spontaneous polarization (~130 μC/cm^2) along the [0001] *c*-axis. However, achieving ferroelectric switching (polarization reversal under an external electric field) typically requires electric fields exceeding its dielectric breakdown strength, rendering such switching impractical under normal conditions. Notably, ferroelectric-like switching has been observed under specific conditions, particularly in ultrathin AlN films, and theoretical studies continue to explore potential switching mechanisms. The feasibility of intrinsic ferroelectricity in pure AlN remains under investigation and appears to depend on factors such as film thickness, strain state, and defect concentration[1-4].

A major breakthrough occurred with the discovery that doping AlN with certain metals can stabilize a ferroelectric phase, significantly reducing the coercive field required for switching while maintaining - or even enhancing - the polarization magnitude. Scandium (Sc), in particular, has proven revolutionary. Alloying AlN with Sc to form $Al_{1-x}Sc_xN$ lowers the coercive field (to < 5 MV/cm) and retains a high remanent polarization (> 100 μC/cm^2), enabling robust switching at voltages compatible with CMOS technologies[5-8]. These properties positioned $Al_{1-x}Sc_xN$ as a leading candidate for next-generation non-volatile memory (NVM) devices, energy harvesting systems, neuromorphic computing, and tunable RF components[9-12]. Beyond scandium, researchers have explored doping AlN with various other metallic elements, including Y, Mg, Ti, Cr, Zr, Nb, Hf, Ta, and W, as well as non-metallic elements such as boron (B)[13-18]. Each dopant uniquely influences the structural, electronic, and ferroelectric properties of AIN, offering a rich design space for materials engineering.

For example, boron doping can induce polarity inversion in AlN, while magnesium codoping has been shown to enhance piezoelectric coefficients. However, to date, its effect on ferroelectric behavior has not been reported[19,20]. These findings highlight the critical interplay between dopant chemistry, lattice distortion, and electronic structure in tailoring ferroelectric responses.

This review provides a comprehensive analysis of the mechanisms underpinning ferroelectric behavior in metal-doped AlN systems, with a focus on Sc-alloyed variants. We analyze the roles of dopant type, concentration, and synthesis methods in determining polarization dynamics and critically assess both experimental findings and theoretical predictions. By synthesizing recent advances, we aim to provide a

roadmap for optimizing doped AlN-based ferroelectrics to meet the demands of future electronic applications.

Ferroelectric switching challenge in pure AlN: challenges and breakthroughs

Although bulk AlN possesses spontaneous polarization, it is not conventionally considered ferroelectric because of the extremely high energy barrier required for polarization reversal via atomic displacements. Theoretical calculations predict coercive fields exceeding 10 MV/cm, often surpassing AIN's dielectric breakdown strength[21]. Consequently, researchers have explored the potential ferroelectricity of undoped AlN. Yasuoka *et al.*[1] reported a polarization-electrical field (P-E) curve for AlN; however, the results were inconclusive, as dielectric breakdown occurred before ferroelectric switching could be verified. In contrast, Lin *et al.*[2] demonstrated ferroelectric behavior in ultrathin AlN films (8-10 nm) prepared via atomic layer epitaxy. They successfully induced ferroelectricity in a single-crystalline epitaxial AlN film of 8-10 nm thickness. This effect was attributed to a unique top-top configuration - two capacitors in series (Pt-AlN-GaN-AlN-Pt) - and the presence of a two-dimensional electron gas (2DEG) at the AlN/GaN interface. The 2DEG formation is driven by out-of-plane compressive and in-plane tensile strain in the [0001]-oriented AlN epilayer. However, this strain-induced mechanism becomes ineffective for thicker films (> 10nm), where the lattice mismatch at the AlN/GaN heterojunction is insufficient to sustain ferroelectricity. Hasegawa *et al.*[3] further demonstrated the possibility of full polarization reversal in pure, undoped AlN at room temperature. By adjusting the deposition temperature from 450 to 250 °C, they achieved complete polarization switching. At 450 °C, local polarization switching and dielectric breakdown occurred before full switching. In contrast, films deposited at 250 °C exhibited significantly higher breakdown fields, enabling full polarization reversal with a remanent polarization of 150 μC/cm² and a coercive field of 8.3 MV/cm. The difference in behavior was attributed to variations in interface quality caused by lattice mismatch. Films deposited at higher temperatures exhibited greater mismatch and trap formation, resulting in lower leakage currents but increased susceptibility to rapid breakdown under high voltage.

Recent breakthroughs in heterostructure engineering have identified alternative strategies for enabling polarization switching in pure AlN without requiring ultrathin films or heavy doping. Skidmore *et al.*[4] showed that interfacial coupling between ferroelectric layers (e.g., $Al_{1-x}Sc_xN$, $Al_{1-x}B_xN$) and adjacent non-ferroelectric AlN layers enables full polarization reversal via proximity effects. This phenomenon is driven by elastic and electric fields generated by propagating domain walls in the ferroelectric layer, which transiently destabilize the AlN lattice and reduce the switching barrier[22,23] [Figure 1]. Proximity-induced ferroelectricity enables polarization switching in micron-thick AlN films (e.g., 500 nm AlN adjacent to 75 nm $Al_{1-x}B_xN$), achieving remanent polarization (P_r) values (~120 μC/cm²) comparable to those of doped systems. Uniform polarity inversion in AlN - excluding defect-mediated artifacts - was confirmed through anisotropic etching, 180° phase shifts in piezoresponse force microscopy (PFM), and scanning transmission electron microscopy (STEM) imaging.

Therefore, achieving polarization reversal in standard AlN films is typically impractical. Drury *et al.*[25] investigated polarization switching in $Al_{0.7}Sc_{0.3}N$ under varying temperatures and found a strong correlation between the coercive field (E_c) and thermal conditions, with E_c decreasing linearly as temperature increases. Their study confirmed stable saturation polarization across the tested temperature range (e.g., up to 400 °C). The polarization-electric field (P-E) loops exhibited a post-saturation negative slope, indicating a reduction in capacitance. This behavior is consistent with the increased current density observed in current-electric field (J-E) sweeps at higher temperatures, which demonstrated an exponential relationship between current density and electric field. Notably, Pr values for $Al_{0.7}Sc_{0.3}N$ showed exceptional thermal stability, while E_c decreased linearly with increasing temperature. This trend is attributed to thermally assisted reductions in the activation energy barrier for polarization reversal. Moreover, the study acknowledged that external

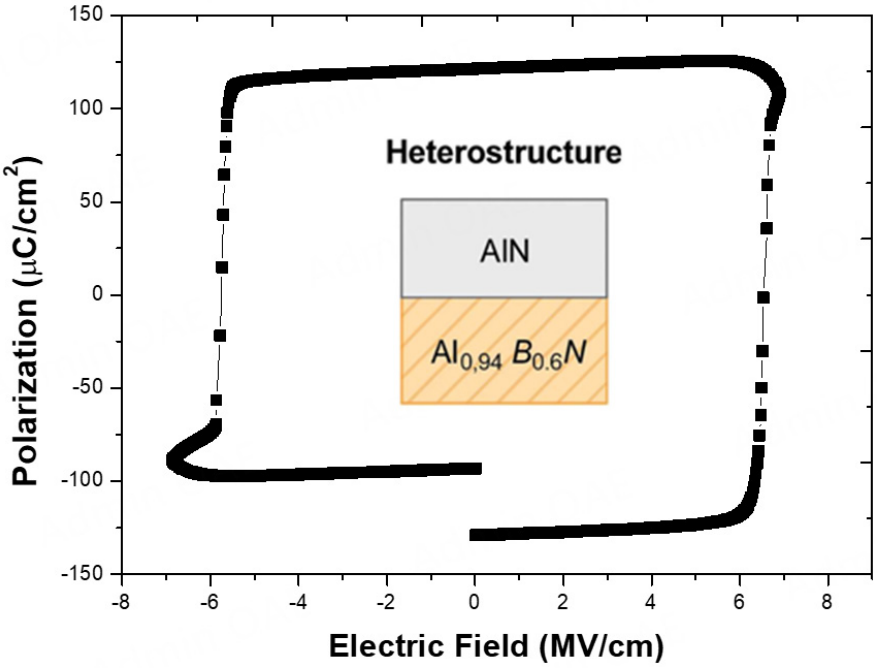

Figure 1. Polarization hysteresis loops for a 200 nm AlN|AlBN bilayer stack[24].

factors such as domain nucleation and growth - both influenced by defects and preferred crystallographic orientation - also affect E_c, particularly in conventional ferroelectric capacitors. While this trend is commonly attributed to thermally assisted domain nucleation and domain wall motion, such an explanation oversimplifies the complex interplay of mechanisms governing polarization switching. A more comprehensive analysis must account for additional factors such as strain relaxation, defect dynamics, and phase boundary interactions, which collectively modulate the switching behavior.

Strain relaxation effects

In epitaxial AlScN films grown on lattice-mismatched substrates (e.g., sapphire or silicon), thermal expansion mismatch induces residual biaxial stress. At elevated temperatures, partial strain relaxation alters the lattice parameters and internal stress state. For example, compressive strain relaxation reduces the energy barrier for polarization rotation by lowering lattice distortion energy. Substrate-induced tensile strain (commonly found in sputtered films) amplifies basal plane expansion at higher temperatures, further softening the wurtzite lattice and promoting polarization reversal through strain-polarization coupling[26-28]. This effect is particularly pronounced in films with high Sc content ($x > 0.3$), where structural flattening (i.e., a reduced c/a ratio) decreases steric hindrance to dipole reorientation.

Defect dynamics

Oxygen-related defects, such as substitutional oxygen impurities (O_N) and associated aluminum vacancies (V_{Al}) introduced during sputtering[29], act as charge traps and domain wall pinning centers. At elevated temperatures, increased defect mobility enables the redistribution of these impurities, reducing their inhibitory effects on domain wall motion. In parallel, nitrogen vacancies (V_N), which have a higher formation energy in AlScN than in AlN, become thermally activated, forming shallow trap states that screen depolarization fields. This defect-mediated screening lowers the effective E_c by compensating for fixed polarization charges at grain boundaries and interfaces[30]. Additionally, the enhanced conductivity at high temperatures - evidenced by exponential J-E behavior - suggests that defect-assisted leakage currents

partially short-circuit the depolarization field, further reducing the switching barrier.

Phase boundary interactions

In mixed-phase regions, thermal energy promotes atomic rearrangement at the interfaces between wurtzite and cubic phases. These interfaces act as nucleation sites for polarization reversal, where the coexistence of polar (wurtzite) and non-polar (cubic) phases creates localized strain gradients. These gradients stabilize intermediate switching states and effectively lower the activation energy for polarization rotation[30]. Furthermore, conductive pathways formed at phase boundaries screen long-range depolarization fields, mimicking the role of mobile charge carriers in classical ferroelectrics. This behavior is analogous to domain wall conductivity observed in oxide ferroelectrics, where metallic-like conduction along domain walls reduces the switching energy[31].

These mechanisms are not mutually exclusive but rather operate synergistically. For example, strain relaxation enhances defect mobility by reducing lattice rigidity, while phase boundary interactions facilitate defect segregation at interfacial regions. This multifaceted interaction helps explain why the reduction in E_c becomes more pronounced and nonlinear at higher Sc concentrations ($x > 0.3$), where structural softening and defect density simultaneously peak.

This understanding opens new avenues for optimizing deposition parameters to achieve higher polarization values and lower coercive fields in undoped AlN. Two main strategies can be considered to address the challenge of reducing E_c. The first involves engineering well-established wurtzite materials such as AlN and ZnO through alloying and strain application[32,33]. The second focuses on the investigation and synthesis of novel wurtzite-type materials that inherently possess lower coercive fields[34,35]. A key objective is to elucidate the underlying polarization switching mechanisms and clarify the structure-property relationships that influence E_c. Ultimately, it is essential to identify structural deviations from the conventional wurtzite configuration that facilitate the transition from positive to negative polarization.

Doping strategies to induce ferroelectricity

Polarization switching refers to the ability of a ferroelectric material to reverse the direction of its spontaneous electric polarization under an applied electric field. This property is critical for numerous electronic applications, including non-volatile memories and sensors[36]. However, the polarization-switching behavior of wurtzite AlN thin films remains poorly defined. Incorporating specific metal cations at the Al sites within the AlN lattice has been shown to effectively reduce the energy barrier for polarization switching.

Boron doping exemplifies how local chemical disorder can stabilize metastable states that are crucial for switching. Studies on $Al_{0.93}B_{0.07}N$ thin films have demonstrated remnant polarization values exceeding 120 $\mu C/cm^2$ and tunable coercive fields ranging from 3.6 to 5.2 MV/cm across a temperature range of 25-200 °C[37]. Unlike scandium, which softens the lattice to reduce switching barriers, B doping introduces bond distortion that stabilizes transient antipolar states during polarization reversal. This mechanism, observed via differential phase contrast scanning transmission electronic microscopy (DPC-STEM)[23,38], aligns with atomic-scale models of polarization switching in wurtzite ferroelectrics. Notably, the wake-up process in B-doped AlN is thermally activated, requiring fewer cycles at elevated temperatures (e.g., < 20 at high temperature *vs.* ~100 cycles at room temperature), with an activation energy of 0.15 ± 0.05 eV[37]. In contrast, the wake-up behavior in Sc-doped AlN is dominated by oxygen vacancy redistribution, highlighting how dopant chemistry influences switching kinetics[39]. DPC-STEM imaging reveals that boron-induced puckering of aluminum/boron-nitrogen rings in the basal planes creates low-energy

pathways for polarization inversion [Figure 2]. These findings bridge local chemical effects (bond distortion) with global structural dynamics (domain propagation), offering a unified model for ferroelectricity in wurtzite structures.

In addition to chemical doping strategies, structural optimization through interlayer (IL) engineering in AlScN ferroelectric diodes has emerged as a promising approach. By incorporating a 0-5 nm AlO_x IL into a metal/ferroelectric/insulator/metal (MFIM) architecture, ON/OFF ratios exceeding 3,000 and rectification ratios above 5,000 were achieved in 10 nm $Al_{0.72}Sc_{0.28}N$ devices[5]. The IL suppresses direct tunneling currents in the high-resistance state while enhancing polarization-driven electrostatic modulation, which is critical for high-density crossbar arrays. This structural optimization mirrors the advantages of defect engineering observed in B-doped systems, effectively addressing leakage issues in scaled geometries. The approach modifies both the crystal structure and electronic interactions, enabling polarization reversal under more accessible electric fields.

However, doping-free approaches that leverage interfacial proximity effects are now emerging as complementary strategies. Traditional methods to induce ferroelectricity in wurtzites, such as Sc or B substitution in AlN[5], introduce scattering centers that degrade thermal and electronic properties. Proximity-induced ferroelectricity circumvents these trade-offs, preserving the pristine characteristics of unmodified AlN and ZnO, which are vital for high-frequency optoelectronics and power devices. This concept builds upon the polar discontinuity model proposed by Stutzmann *et al.*[22] for GaN/AlN junctions, extending it to demonstrate dynamic reconfigurability rather than relying solely on static polarization engineering. For example, hybrid nitride-oxide stacks (e.g., AlBN/ZnO) exhibit a reduced coercive field (E_c = 3.2 MV/cm) compared to standalone AlBN (E_c = 5.8 MV/cm), highlighting the synergistic enhancement of interfacial electric fields[4] [Figure 3]. This mechanism avoids the drawbacks of alloying (e.g., oxygen-related defects in sputtered AlScN) while preserving the electronic integrity of undoped AlN or ZnO[22,38].

The type and concentration of a dopant can influence the polarity of a film, the magnitude of its polarization, and its switching behavior. For example, doping wurtzite AlN with Si can invert the film's polarity from Al-polar to N-polar. Ge doping can also reverse the polarity, although the resulting switching behavior differs. In contrast, Mg doping increases the magnitude of polarization without altering the film's polarity. Various switching mechanisms have been proposed for wurtzite AlN thin films, including domain wall motion, charge injection, and defect-assisted switching. Different dopants can affect these mechanisms in distinct ways. For example, Si doping promotes the formation of domain walls, thereby enhancing switching behavior. Ge doping, on the other hand, facilitates charge injection, which also contributes to improved switching performance. Aluminum scandium nitride ($Al_{1-x}Sc_xN$) is a ternary compound with a wurtzite crystal structure similar to that of AlN. However, as the ionic radius of Sc is larger than that of Al, Sc incorporation causes lattice distortion in the $Al_{1-x}Sc_xN$ wurtzite structure. This distortion significantly impacts the compound's properties, particularly its optical and ferroelectric characteristics.

Metal dopants can be classified into two performance tiers based on their ability to optimize key ferroelectric parameters: P_r and E_c. Sc-doped AlN, the focal point of this analysis, falls into the high-performance tier due to its exceptional ability to achieve $P_r \geq 100$ μC/cm² and reduce E_c to ≤ 5 MV/cm at moderate doping levels (x~0.3). This performance surpasses that of alternative rare earth dopants, such as yttrium (Y), lanthanum (La), and certain transition metals (e.g., Mg, Zn). For instance, $Al_{1-x}Y_xN$ can reach $P_r \approx 80$ μC/cm² at x = 0.25 but requires $E_c \approx 6$ MV/cm to switch polarization, which limits compatibility with CMOS technology. $Al_{1-x}La_xN$ requires x > 0.4 to achieve $P_r \approx 90$ μC/cm², but the large ionic radius of La^{3+}

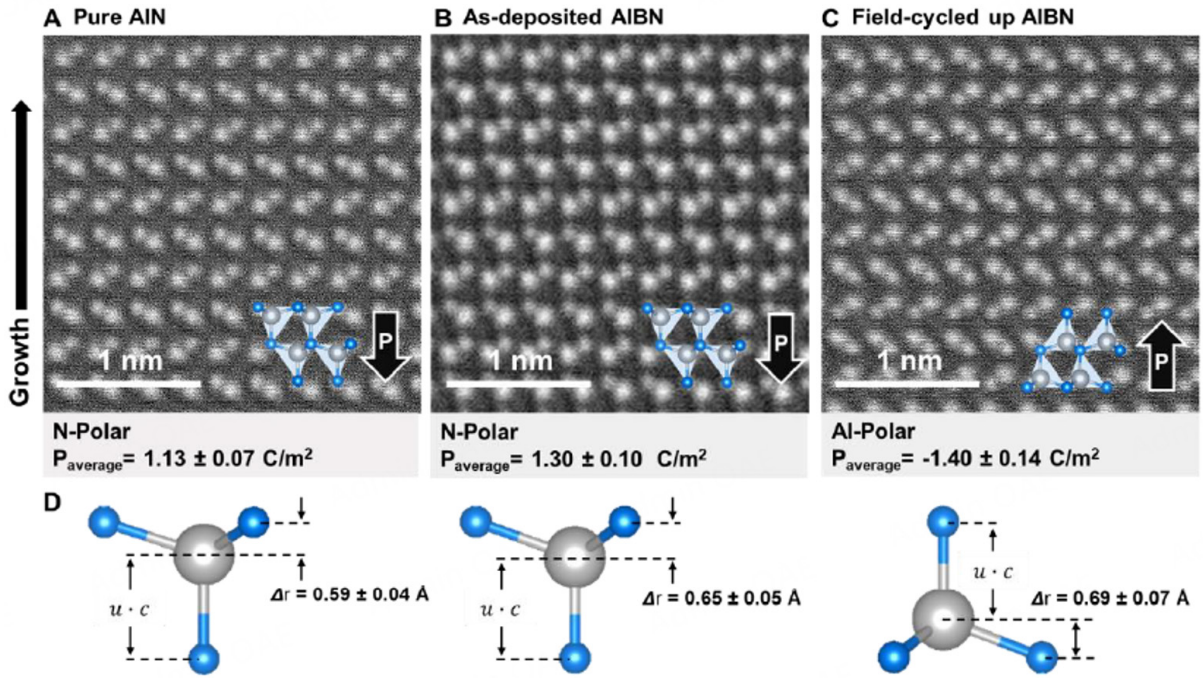

Figure 2. (A-C) dDPC images for pure AlN, as-deposited $Al_{0.94}B_{0.06}N$, and field-cycled $Al_{0.94}B_{0.06}N$. (D) Schematic of structural modifications following boron incorporation and field cycling[23].

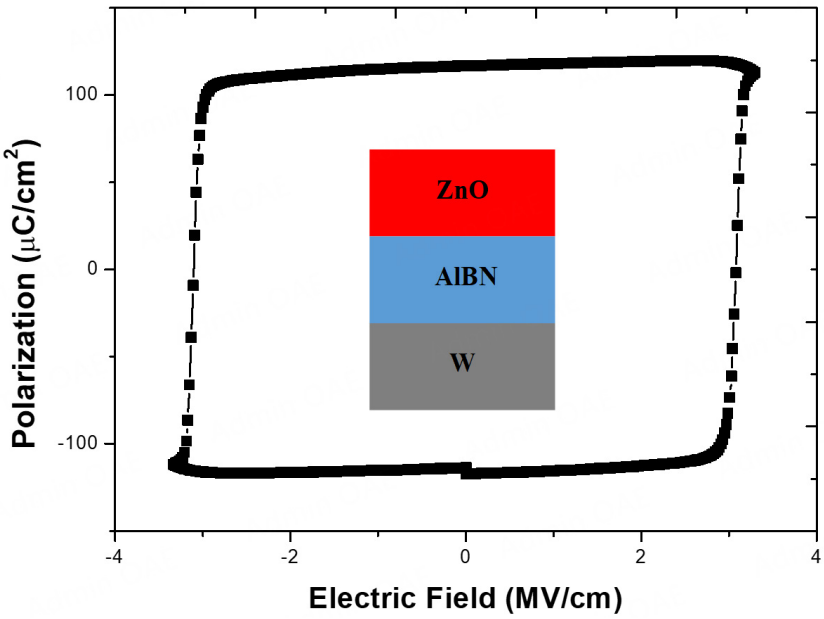

Figure 3. Polarization hysteresis loops for a heterojunction capacitor comprising 250 nm ZnO/200 nm $Al_{0.94}B_{0.06}N$/100 nm W[24].

(1.17 Å *vs.* Al^{3+}: 0.54 Å) introduces excessive lattice strain, destabilizing the wurtzite phase and leading to cubic inclusions and E_c > 8 MV/cm)[40]. The superior performance of Sc is attributed to its optimal ionic radius (Sc^{3+}: 0.88 Å, compared to Y^{3+}: 1.04 Å and La^{3+}: 1.17 Å) and lower electronegativity (1.36 *vs.* 1.22 for Y and 1.10 for La), which together help balance lattice distortion and bond ionicity. Sc doping reduces the c/a ratio by ~1.5% at x = 0.3, lowering the energy barrier for polarization switching by 40% compared to Y-

doped systems[35,40]. In contrast, the larger ionic radius of La destabilizes the wurtzite phase at lower concentrations ($x > 0.2$), promoting cubic phase formation and degrading the ferroelectric response. These findings define the performance threshold for higher-tier dopants as those that can achieve $P_r \geq 100$ μC/cm² and $E_c \leq 5$ MV/cm without phase segregation at doping levels below $x = 0.5$[41]. Scandium uniquely satisfies these criteria, likely due to localized bond frustration and the possible stabilization of a metastable hexagonal phase during switching.

In comparison, dopants such as Mg and Zn are categorized in the standard performance tier. Although well-established and widely used, these dopants generally fail to meet the performance requirements for applications demanding high efficiency and low power consumption. The selection of a dopant involves a complex trade-off among several factors, including cost, process compatibility, and device performance. While Sc-doped AlN offers superior efficiency, its higher cost and potential fabrication challenges may limit widespread adoption. Nevertheless, recent research has demonstrated methods to reduce the switching voltage in $Al_{1-x}Sc_xN$ films by modifying the material structure or experimental setup. Strategies include adjusting the testing temperature[42], increasing the Sc content[1], enhancing crystallinity[43,44], and employing alternative substrates[6] - all of which have shown effectiveness in lowering the required switching voltage while maintaining high polarization values. As these technologies mature, the cost of $Al_{1-x}Sc_xN$ is expected to decline, making it more viable for commercial applications.

$Al_{1-x}Sc_xN$ exhibits superior properties compared to traditional aluminum nitride (AlN), including an enhanced piezoelectric coefficient and improved electromechanical coupling, owing to the substitution of Al with Sc[45]. This material overcomes the ferroelectric limitations of AlN thin films while maintaining excellent high-temperature stability, CMOS compatibility, and mechanical robustness[46]. Like AlN, $Al_{1-x}Sc_xN$ has a wurtzite crystal structure, with atoms arranged in a hexagonal pattern[47]. Wurtzite-structured doped III-nitrides offer significant advantages, such as scalability, compatibility with existing manufacturing procedures, and strong ferroelectric performance. These materials are well-suited for large-scale applications, such as displays and memory devices, and can be fabricated using established III-V semiconductor processing techniques[48-51]. Moreover, their strong ferroelectric properties make them ideal candidates for high-performance electronic applications. However, the exact origin of ferroelectric behavior in $Al_{1-x}Sc_xN$ wurtzite structures remains incompletely understood. It is believed to be influenced by several factors, including the local chemical environment, extended structural characteristics, and the presence of intrinsic defects.

In addition to the ferroelectric response in doped III-N wurtzite structures being of interest to researchers for three main reasons, several other factors contribute to their growing appeal. One notable advantage is their tunable properties[52], which can be modulated by adjusting the type and concentration of dopants as well as the growth conditions. This tunability makes them highly versatile for tailoring specific ferroelectric characteristics. Furthermore, doped III-N wurtzite materials can be integrated with other III-V semiconductors and silicon[13], making them promising candidates for heterogeneous integration - an essential technology for future electronic devices. Among these materials, $Al_{1-x}Sc_xN$, which possesses a distinct wurtzite structure, exhibits limitations for certain applications. In particular, its piezoelectric coefficient is relatively low compared to alternative materials, which restricts its applicability. Nevertheless, the thin-film piezoelectric device market is rapidly expanding. According to the Business Research Company, this market was valued at approximately $3,860.5 million and is projected to reach $17,663.98 million by 2032, with a compound annual growth rate of 14.8%[53]. A study investigating the dependence of piezoelectricity on elemental combinations in $A_{0.5}B_{0.5}N$ (A = Sc, Y, La; B = Al, Ga, In)[40] found significant enhancements in the piezoelectric constants when Sc, Y, and La were substituted into AlN,

GaN, and InN, respectively. The enhancement is attributed to the substitution of A-site elements (Sc, Y, or La), which have larger ionic radii than B-site elements (Al, Ga, or In). This difference in size leads to greater polarization within the material, thereby amplifying the piezoelectric response. The enhanced piezoelectric properties in doped III-N wurtzite structures, such as Sc-substituted AlN ($Al_{1-x}Sc_xN$), result from a complex interplay of ionic polarization, lattice distortion, and electronic structure modifications. Substituting a larger cation (e.g., Sc^{3+} with an ionic radius of ~0.61 Å in tetrahedral coordination) for a smaller one (Al^{3+}, ~0.39 Å) induces considerable lattice strain. This strain reduces the local symmetry of the wurtzite structure, thereby amplifying internal polarization. This behavior is described by the piezoelectric constitutive relation:

$P_i = d_{ijk}\sigma_{jk} + \varepsilon_{ij}E_j$, where the piezoelectric coefficient d_{ijk} depends on the material's Born effective charge (Z^*), elastic compliance, and polarization susceptibility. Sc^{3+} substitution elongates the cation-anion bond length (e.g., Sc-N *vs.* Al-N), increasing bond polarizability and enhancing Z^*, which reflects the dynamic contribution to polarization per unit atomic displacement. Additionally, lattice distortion alters the electronic structure, further impacting Z^*. The resulting dipole moment ($\mu = Z^* \cdot \delta r$), where δr is the relative ion displacement under strain, increases due to both a higher Z^* and a larger δr, the latter resulting from softer bonds in the strained lattice. Together, these factors significantly enhance the intrinsic piezoelectric response under applied stress. Moreover, the enhancement of piezoelectricity in ABN compounds also depends on the type of B-site element. The highest piezoelectric constants are observed in systems where Al is the B-site element, followed by Ga and In. This trend is attributed to the stronger covalent bonding in Al-N compared to the more ionic nature of Ga-N or In-N. Strong covalent bonds in Al-N enable structural integrity under strain while allowing reversible ionic displacement. In contrast, Ga-N and In-N bonds reduce lattice rigidity and increase inharmonic phonon scattering, thereby dissipating piezoelectric energy. However, achieving high concentrations of A-site dopants (e.g., in $Al_{1-x}Sc_xN$ with $x > 0.5$) is constrained by phase instability. At elevated Sc content, the metastable wurtzite phase tends to transition to a non-piezoelectric cubic phase. It has been predicted that a higher piezoelectric effect can be achieved at higher Sc ratios if the wurtzite phase can be stabilized against this transformation. This stabilization may be facilitated by introducing a third dopant element, which could reduce coherency strain and suppress cation migration, thereby extending the compositional range conducive to high piezoelectricity. This highlights the need to balance ionic size mismatch, bond strength, and phase stability to optimize electromechanical coupling in nitride-based piezoelectrics. In this context, the use of a seed layer offers a viable strategy. According to Höglund *et al.*[54], (cubic)-$Al_{1-x}Sc_xN$ solid solutions deposed using ScN seed layers can be synthesized with AlN molar fractions up to ~60%. The transition from a mixed-phase (wurtzite + cubic) to a purely cubic phase occurs at around $x \approx 0.5$, depending on the specific seed layer and growth conditions.

Furthermore, the large-scale fabrication of doped AlN remains challenging and must be addressed to enable commercial viability. These challenges have limited the development of AlN - particularly doped wurtzite films such as $Al_{1-x}Sc_xN$ - for use in piezoelectric, ferroelectric, and FeRAM applications. Notably, although sputter deposition is commonly employed for AlN films in these applications due to its compatibility with CMOS processes, residual oxygen or water vapor in vacuum chambers can introduce oxygen-related defects (e.g., Al vacancies and O substitution), which disrupt crystallinity and increase leakage currents, ultimately compromising device reliability[29]. Temperature-dependent I-V analysis confirms that Poole-Frenkel emission ($J \propto e^{-1/T}$) dominates the low-resistance state, while thermionic emission ($J \propto T^2 e^{-1/T}$) governs the high-resistance state at low biases[5]. These phenomena necessitate ultra-high vacuum (UHV) conditions ($< 10^{-7}$ Torr) and advanced chamber passivation techniques, both of which significantly raise production costs and complicate scalability. Despite these obstacles, advancements in scaled AlScN devices have led to the successful demonstration of 5 nm $Al_{0.72}Sc_{0.28}N$ ferroelectric diodes with CMOS back-end-of-line (BEOL) compatibility (< 400 °C processing). These devices exhibit 32 distinct memory states (5-bit operation), an

ON/OFF ratio > 1,175, and retention stability > 300 s[5]. However, depolarization fields in sub-10 nm devices continue to degrade retention (e.g., a 5 nm AlScN/2 nm AlO_x stack lost retention after 2,500 s), highlighting the need for high-k IL materials in future device optimization. Moving forward, improving AlN film quality, refining growth conditions, and enhancing material properties will be essential to achieving industrial-scale commercialization. Researchers are actively working to address these challenges and to develop new methods for synthesizing and stabilizing the wurtzite structure. One such strategy involves doping $Al_{1-x}Sc_xN$ with elements such as Ga or In, which has been shown to stabilize the wurtzite phase and improve material properties. Another promising technique is epitaxial growth - growing thin films on substrates with differing crystal structures - which has demonstrated potential in stabilizing desirable phases[26]. Doping AlN remains challenging due to the formation of deep-level defects in the band gap and the complex interactions between intrinsic ionic and electronic defect disorders. For example, to address the challenges associated with n-type doping, dos Santos *et al.*[55] investigated gas-phase reactions driven by silane (SiH_4), a dopant precursor used in metal-organic chemical vapor deposition (MOCVD). Through computational modeling, they identified potential dopant species, such as $(CH_3)_2AlSiH_3$ and H_2NSiH_3, which contain Al-Si and N-Si bonds and form through reactions involving trimethylaluminum, ammonia, and silane. These species are proposed to play a key role in incorporating silicon into the AlN film during deposition. This study advances our understanding of AlN doping mechanisms and may lead to improved fabrication methods for doped AlN-based devices. Metal dopants are typically classified into two performance tiers based on their influence on AlN polarization properties. Scandium-doped AlN, the primary focus of this study, falls into the "High-Performance" tier due to its outstanding ability to enhance residual polarization and reduce switching energy. In contrast, dopants such as Mg and Zn are categorized under the "Standard Performance" tier. Although these dopants are well-established and widely used, they often fall short of meeting the performance criteria required for high-efficiency, low-power applications. Ultimately, the choice of dopant is a multifaceted decision influenced by several factors, including cost-effectiveness, processing complexity, and targeted device performance.

Al-Sc-N system: the leading candidate

Incorporating specific metal cations into Al sites within the AlN lattice has proven effective in lowering the energy barrier for polarization switching, thereby inducing or stabilizing ferroelectricity. This strategy modifies the crystal structure and electronic interactions, enabling polarization reversal under accessible electric fields. Among the dopants explored, Sc has garnered the most attention due to its dual role in disrupting local chemical bonding and inducing global structural distortions. Other dopants have also been investigated, leading to a broad family of ferroelectric wurtzite nitrides.

AlN is a III-V compound semiconductor, composed of aluminum from group III and nitrogen from group V of the periodic table. This composition imparts AlN with a wide range of functional properties, especially in optoelectronic applications[56]. AlN typically crystallizes in the wurtzite phase, where each Al atom is tetrahedrally coordinated to four nitrogen atoms through covalent bonds [Figure 4].

In the AlN wurtzite structure, the bond along the c-axis (0001 direction), referred to as B_2, is slightly longer (1.90 Å) than the three equivalent B_1 bonds (each 1.89 Å). This subtle asymmetry highlights the non-centrosymmetric nature of the AlN unit cell, a key factor underlying its piezoelectric behavior. Even in the absence of external electrical or mechanical stimuli, AlN films exhibit a spontaneous polarization in their charge distribution. The wurtzite phase represents the thermodynamically stable configuration of AlN. Due to the polarity along the [0001] and [000-1] directions, surface terminations can be either Al-polar or N-polar. In Al-polar surfaces, aluminum atoms are positioned at the top of the diatomic layer, while in N-polar surfaces, nitrogen atoms occupy the apex. For Al-polar configurations, the c-axis aligns with the internal electric field extending from the substrate to the surface, resulting in a polarization direction

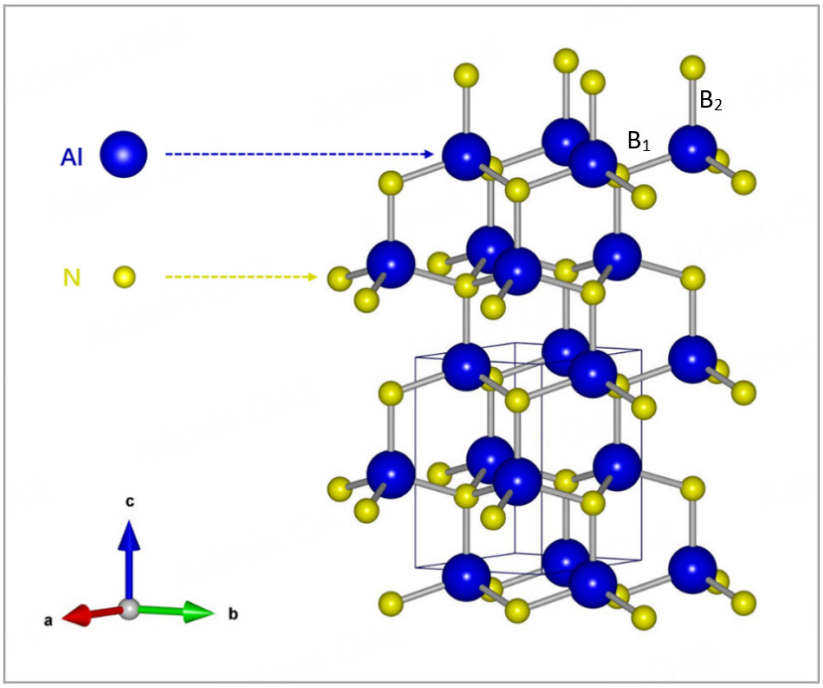

Figure 4. Crystalline structure of AlN in the wurtzite phase.

opposite to the field. This leads to positive polarization-induced fixed charges at the substrate interface and negative charges at the surface. In contrast, this relationship is reversed for N-polar surfaces.

AlN exhibits a spontaneous polarization of approximately 0.08 C/m^2[57], confirming its pyroelectric nature. Its specialized crystalline structure offers excellent thermal and chemical stability, high thermal conductivity (~320 W/m•K), and a melting point of around 2,800 K, which exceeds that of zinc-blende AlN (2,387 ± 300 K). These properties make AlN a superior piezoelectric material for high-temperature surface acoustic wave sensors[58]. As a III-V semiconductor with a wide bandgap (~6 eV), AlN is also explored for ultraviolet light-emitting diodes. However, its piezoelectric properties can degrade due to surface oxidation, which begins at around 700 °C in ambient air[59].

Structure evolution and phase transition in $Al_{1-x}Sc_xN$

The substitution of aluminum atoms in AlN with scandium was first intensively studied by a Japanese team. They demonstrated that $Al_{1-x}Sc_xN$ films (0.1-1.1 μm thickness, x = 0.43) exhibit a significantly enhanced piezoelectric coefficient, with d_{33} increasing from 5.5 pC/N for pure AlN to 27.6 pC/N for $Al_{1-x}Sc_xN$ - a fivefold improvement[60]. Structural analysis indicates that Sc has limited solubility in AlN, resulting in three distinct phases depending on Sc concentration:

• Wurtzite phase for $x < x_1$

• Mixed phase (wurtzite + cubic) for $x_1 < x < x_2$

• Cubic phase for $x > x_2$

The bandgap evolution in AlScN as a function of Sc content can indicate possible structural transitions. Deng *et al.*[61] demonstrated that the optical absorption spectra of $Al_{1-x}Sc_xN$ films, grown on sapphire (0001) substrates via reactive magnetron co-sputtering, exhibited a nearly linear decrease in bandgap energy for $x < 0.20$. Similarly, Jin *et al.*[62] reported a significant reduction in the bandgap from 4.37 to 2.94 eV over the same range, stabilizing beyond $x > 0.34$. This bandgap narrowing may be attributed to absorption contributions from segregated ScN phases, which reduce the apparent optical bandgap of AlScN - similar to the behavior observed in GaScN for x values between 0.30 and 0.50[63]. Theoretically, the optical bandgap of AlScN remains direct up to $x \approx 0.25$. As Sc content increases beyond this point, the bandgap becomes indirect due to the influence of Sc 3d states on the conduction band minimum of $Al_{1-x}Sc_xN$. This results in flatter electron dispersion and reduced energy gaps[51]. For reference, ScN in its rocksalt structure has an indirect bandgap of 0.9 eV, highlighting Sc's significant impact on the alloy's electronic structure[64].

Dual mechanisms of ferroelectric enhancement

Doping AlN with Sc (or alloying it with ScN) significantly enhances its ferroelectric response through two distinct mechanisms:

- Local chemical bonding effects: The larger ionic radius of Sc^{3+} (0.88 *vs.* 0.54 Å for Al^{3+}) disrupts the covalent sp^3 bonding network of AlN, causing bond frustration. Sc prefers octahedral coordination (via sd^3 hybridization) over tetrahedral, introducing localized strain fields that lower the Peierls-Nabarro barrier for domain wall motion.

- Global structural flattening: Increasing Sc content reduces the c/a ratio of the wurtzite lattice, promoting a flatter structure and enabling polarization rotation via a proposed metastable hexagonal (H) phase.

Höglund *et al.*[27] investigated $Al_{1-x}Sc_xN$ films through structural characterization and first-principles calculations for x values from 0 to 0.78. Their results indicated the formation of a disordered single-crystal solid solution in the wurtzite phase (w-$Al_{1-x}Sc_xN$), with a solubility limit of ScN in AlN at 22%. For $x < 0.22$, the c-parameter remains nearly constant, while the a-lattice parameter increases linearly due to the larger Sc ionic radius. Specifically, the a-parameter increases from 3.11 to 3.21 Å as x increases from 0 to 0.22, while the c-parameter shows minimal change. As Sc content increases between 23% and 50%, nanocrystalline mixtures of ScN and AlN form, and at higher concentrations, a cubic $Al_{1-x}Sc_xN$ phase becomes dominant. Notably, in the composition range $0.4 < x < 0.55$, the wurtzite, cubic, and hexagonal phases can coexist. Increasing Sc content also leads to a decline in crystal quality due to higher defect intensities and local deformations. Nonetheless, the films maintain a disordered single-crystal solid solution structure, with randomly distributed Al and Sc atoms - typical of ternary alloys - and this randomness is believed to enhance the piezoelectric performance of $Al_{1-x}Sc_xN$.

The effect of Sc concentration on the piezoelectric properties of $Al_{1-x}Sc_xN$ provides insights into the origins of ferroelectric behavior. Using first-principles calculations, Tholander *et al.*[65] and Tasnádi *et al.*[45] found that the enhanced piezoelectric response is intrinsically linked to local coordination competition in different environments, driven by the metastable layered hexagonal phase of ScN. Polarization changes primarily result from lattice distortions surrounding Sc sites, underscoring the importance of local atomic environments. At $x = 0.5$, the observed peak in piezoelectric constants is attributed to strong competition between Al and Sc atoms for bonding with nitrogen, particularly between the h-ScN and α-AlN phases. Sc's preference for hexahedral coordination introduces structural frustration, amplifying the material's response to strain. Thus, the hexagonal structure of ScN plays a crucial role in enhancing piezoelectricity, confirming

that intrinsic alloy effects are the primary drivers of the observed improvements in $Al_{1-x}Sc_xN$.

Umeda *et al.*[66] performed first-principles calculations and experiments to study the structural and piezoelectric properties of $Al_{1-x}Sc_xN$ alloys. They observed that increasing the Sc concentration led to a reduction in the c/a lattice ratio, which corresponds to an increase in the hexagonal structure parameter. This parameter reflects the ratio between the bond length along the c-axis and the c-lattice constant, effectively characterizing the interplanar distance between metal and nitrogen atoms. Experimentally, for Sc concentrations up to 0.5, they reported a linear increase in the c-lattice constant up to a Sc ratio of 0.2, followed by a rapid decrease up to 0.4. This structural flattening (i.e., reduction in the c/a ratio) was found to correlate with enhanced piezorelectric coefficients d_{33} and d_{31}, which was attributed to increased mobility of Al atoms along the c-axis[66]. Electron probe microanalysis revealed that scandium substitution reduces the spatial occupancy of Al atoms, causing lattice distortion during the phase transition process[67]. This transition from a hexagonal to a cubic structure induces a 14-fold increase in the piezoelectric coefficient. However, when the scandium concentration exceeds x = 0.3, the cubic structure becomes energetically more favorable, leading to a sharp decline in piezoelectric response. They suggest that the maximum piezoelectric response occurs in a mixture of polar wurtzite AlN and non-polar cubic ScN (if the wurtzite structure is maintained). This is plausible because the polar wurtzite structure exhibits piezoelectricity, while the cubic structure does not. The authors believe that combining these two structures could yield material benefits from both the piezoelectric properties of wurtzite and the structural stability of the cubic phase. However, this remains a theoretical concept, as no experimental studies have yet succeeded in creating such a material. Further research is required to determine whether this can be achieved.

The phase transition from wurtzite to cubic rocksalt also reveals discrepancies between Density Functional Theory (DFT) predictions and experimental observations. DFT calculations, such as those by Talley *et al.*[68] (x = 0.64) and Furuta *et al.*[69] (x = 0.67), predict a sharp compositional threshold for the phase transition under equilibrium conditions. In contrast, experiments consistently reveal mixed-phase coexistence (wurtzite and cubic) during the transition, influenced by scandium concentration, deposition parameters, substrate properties, and kinetic effects. These discrepancies arise from inherent differences between idealized theoretical models (which assume equilibrium and defect-free systems) and real-world synthesis methods such as magnetron sputtering, where rapid growth rates and limited adatom mobility prevent complete atomic rearrangement and stabilize metastable mixed phases.

Additionally, defects (e.g., vacancies, dislocations) and substrate-induced strain fields can act as nucleation sites for cubic domains or disrupt long-range ordering, thereby promoting phase coexistence. Experimental systems also face thermodynamic limitations: while DFT predicts phase separation into AlN and ScN due to the positive mixing enthalpy, kinetic freezing during deposition traps Sc in a metastable solid solution. Substrate interactions add further complexity. For example, epitaxial strain from sapphire (0001) can stabilize cubic phases at lower x or alter lattice parameters, resulting in deviations from bulk predictions. Moreover, configurational entropy at deposition temperatures (absent from 0 K DFT models) contributes to the stabilization of disordered alloys. Post-deposition annealing studies highlight the role of kinetics: prolonged thermal treatment reduces mixed-phase regions, bringing experimental outcomes closer to DFT predictions. Thus, the discrepancies between theory and experiment reflect a complex interplay of thermodynamic driving forces, kinetic limitations, defect dynamics, and strain engineering, factors that are critical for optimizing the functional properties of AlScN in next-generation electronic devices. DFT's reliance on periodic boundary conditions and simplified supercell approximations limits its ability to capture nanoscale heterogeneity and localized strain gradients observed in experimentally observed mixed-phase systems. Höglund *et al.* conducted *ab initio* calculations to assess the mixing enthalpy of wurtzite

AlN, rocksalt ScN, and layered hexagonal ScN[27]. Their results indicate that AlScN transitions from a hexagonal to a cubic rocksalt structure at $x \approx 0.56$. However, the positive mixing enthalpy suggests thermodynamic instability, favoring phase separation into pure AlN and ScN. Despite this, kinetic limitations (e.g., low diffusion rates during growth) and defect-stabilization mechanisms allow the metastable phase to persist. For example, Sc-rich clusters or interfacial strain at grain boundaries can locally stabilize cubic regions even below the theoretical transition threshold. These factors, combined with deposition-specific parameters (e.g., nitrogen partial pressure, substrate bias), create a complex energy landscape where phase evolution is pathway-dependent rather than purely composition-driven. Understanding these dynamics is essential for device fabrication, as the coexistence of wurtzite and cubic phases in the $0.4 < x < 0.55$ range offers unique electromechanical properties - requiring precise process control to optimize phase purity and performance.

The disparity between DFT and experimental observations in $Al_{1-x}Sc_xN$ phase transitions stems from the combined effects of kinetic limitations, defect dynamics, strain, and entropy - factors often omitted in theoretical models. A holistic understanding requires the integration of *ab initio* insights with mesoscale phenomena (e.g., defect distributions, strain relaxation) and process-dependent kinetics. Advances in computational methods, such as machine-learning force fields and phase-field modeling, could bridge this gap by simulating larger-scale, defect-laden systems under non-equilibrium conditions. Experimentally, *in situ* characterization during growth (e.g., XRD, TEM), paired with controlled annealing studies, will further elucidate the kinetic pathways governing phase evolution, enabling the precise tuning of AlScN's functional properties.

Ferroelectric behavior and polarization switching

The first demonstration of ferroelectricity in the III-V semiconductor AlN doped with Sc was reported by Fichtner *et al.*[46], providing evidence that the observed P-E hysteresis loops result from true ferroelectric behavior. Specifically, the wurtzite crystal structure is conserved during the application of a switching field, and polarization switching occurs at the unit-cell level in $Al_{1-x}Sc_xN$. This switching process involves the cooperative displacement of Al^{3+}/Sc^{3+} cations relative to the N^{3-} sublattice within a softened double-well potential energy landscape. While undoped AlN requires a coercive field higher than its breakdown strength to reverse polarization, increasing the Sc content significantly lowers this barrier. For instance, the coercive field decreases from 5 MV/cm in $Al_{0.73}Sc_{0.27}N$ ($x = 0.27$) to below 2 MV/cm in $Al_{0.57}Sc_{0.43}N$ ($x = 0.43$), while maintaining a remanent polarization exceeding 100 μC/cm^2[46]. Lu *et al.*[70] further investigated the field-dependent switching dynamics in 20-nm-thick $Al_{0.72}Sc_{0.28}N$ capacitors, revealing a transition from nucleation-limited switching (NLS) at low electric fields ($< 1.5\ E_c$) to Kolmogorov-Avrami-Ishibashi (KAI)-like kinetics at higher fields ($> 1.5\ E_c$). Similar frequency-dependent polarization dynamics are observed in B-doped AlN ($Al_{0.93}B_{0.07}N$), where the time under an applied field (cycles/frequency) governs the wake-up behavior[37]. This phenomenon is driven by an unusually high activation field ($\alpha \sim 126$ MV cm^{-1}), two orders of magnitude larger than that of perovskite ferroelectrics such as $Pb(Zr,Ti)O_3$. As a result, switching times can be reduced by 5-6 orders of magnitude with only moderate field increases (1.2-2 E_c)[37,71]. These ultrafast switching kinetics, attributed to Sc-induced lattice softening and defect-mediated nucleation, underscore the potential of AlScN for high-speed, non-volatile memory applications.

Studies on epitaxial AlScN/GaN heterostructures further highlight the interplay between interfacial stability and polarization dynamics. Wang *et al.* demonstrated that $Al_{0.82}Sc_{0.18}N$ undergoes rapid surface oxidation upon air exposure[72], forming a disordered oxide layer rich in Sc-O and Al-O bonds.

This oxidation introduces a secondary valence band edge at ~6 eV in XPS measurements, complicating the accurate determination of intrinsic band alignment. However, when samples are maintained under vacuum, the intrinsic type-II band alignment of $Al_{0.82}Sc_{0.18}N$/GaN is preserved, revealing a valence band offset of 0.2 eV and a conduction band offset of 2.3 eV. This alignment enables strong two-dimensional electron gas (2DEF) confinement at the heterointerface, with simulations predicting a 385% increase in sheet carrier density compared to conventional $Al_{0.3}Ga_{0.7}$/GaN. The lattice-matched, strain-free interface minimizes dislocation-mediated leakage and enhances electron mobility by reducing alloy disorder scattering. These findings position AlScN/GaN as a promising platform for high-electron-mobility transistors (HEMTs) and photodetectors, though the rapid oxidation kinetics necessitate stringent environmental controls during device fabrication.

The reduction in switching barriers is theorized to involve metastable hexagonal phase intermediates that emerge during polarization rotation. Although direct experimental evidence for this phase in pure AlN remains lacking - due to its high formation energy - recent atomic-scale studies on $Al_{0.94}B_{0.06}N$ thin films using differential phase contrast scanning transmission electron microscopy (DPC-STEM) have confirmed the presence of such intermediate states. These studies reveal a transient nonpolar geometry during the switching process [Figure 5][23].

In Al-B-N systems, polarization reversal proceeds through a sequential antipolar phase that reduces the switching barrier by 60% compared to pure AlN. First-principles simulations corroborate this mechanism, showing that alloying elements such as B or Sc introduce bond frustration and stabilize transient states, thereby enabling domain wall nucleation and propagation under lower electric fields[38].

Further direct evidence of this mechanism comes from piezoresponse force microscopy (PFM) imaging by Lu *et al.*[70], who observed domain nucleation rates as high as 10^{14} m^{-2} and domain wall velocities ranging from 10^{-4} m/s (4.5 MV/cm) to 1 m/s (6.5 MV/cm). These observations align with DFT predictions of transient nonpolar states during switching[73]. Partial polarization reversal generates polydomain states with inclined 180° domain walls, which Lu *et al.*[70] demonstrated to enhance steady-state conductance by up to two orders of magnitude compared to monodomain configurations [Figure 6].

This phenomenon, attributed to conductive domain walls acting as nanoscale current pathways, mirrors STEM observations in $Al_{0.74}Sc_{0.26}N$[6] and aligns with theoretical models of conductivity induced by polarization discontinuities. Atomic-scale evidence of polarization reversal mechanisms in wurtzites was provided by Schönweger *et al.*[6], who used aberration-correction STEM to visualize inclined 180° inversion domain boundaries (IDBs) within single-nanometer grains of $Al_{0.74}Sc_{0.26}N$ [Figure 7].

These IDBs exhibit horizontal polarization discontinuities, challenging classical vertical domain wall models. The presence of sub-grain domains supports analog-like switching via domain wall motion, a feature essential for neuromorphic computing. Notably, partial polarization reversal within grains enables multi-state operation - a phenomenon previously theorized but not yet observed in wurtzite systems.

However, ferroelectricity is stable only within a limited Sc concentration range ($x < \sim 0.5$). Beyond this threshold, excessive Sc incorporation destabilizes the wurtzite structure, leading to phase segregation or a transition to non-ferroelectric cubic phases, thereby suppressing switchable polarization. The coercive field can also be modulated by increasing tensile strain, for instance by adjusting the Ar partial pressure in the sputter gas. Tensile strain amplifies basal plane expansion, reducing switching barriers through strain-polarization coupling. These findings establish $Al_{1-x}Sc_xN$ as a tunable ferroelectric system - provided the Sc content remains below its phase-stability limit ($\sim x = 0.5$) - paving the way for novel III-N-based ferroelectric devices.

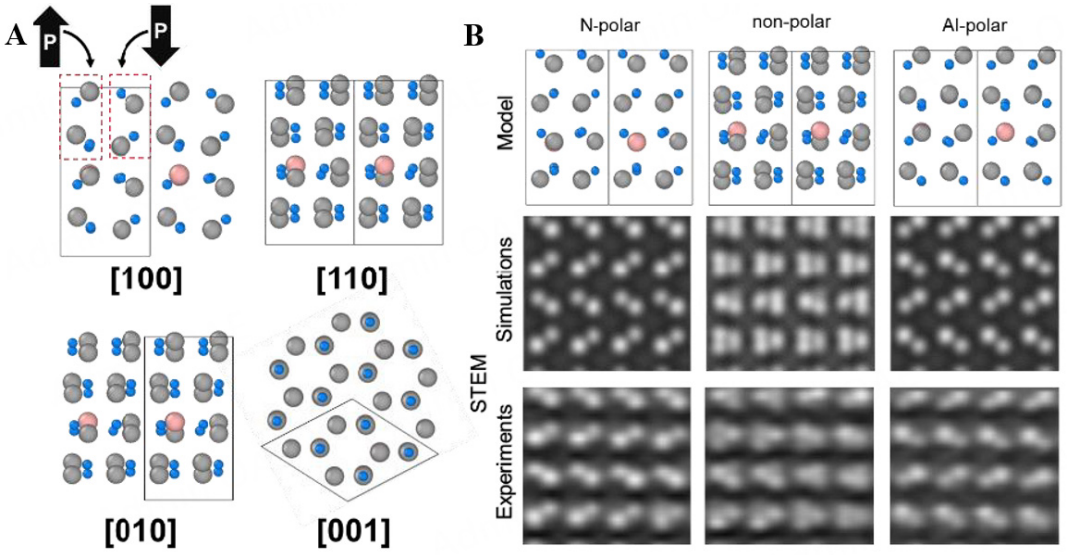

Figure 5. Nudged-elastic-band simulation of polarization reversal pathways. (A) Structural model of the nonpolar transient state calculated for $Al_{15/16}B_{1/16}N$, viewed along different projections. (B) Atomic models, STEM image simulations, and experimental images of the N-polar, nonpolar and Al-polar states[23].

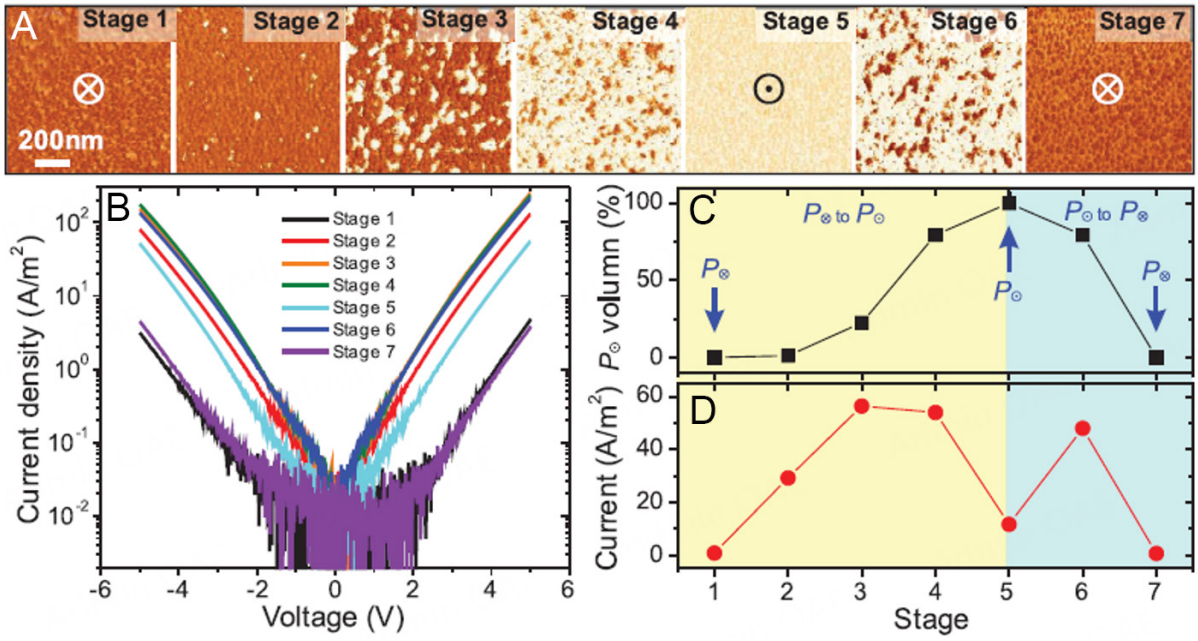

Figure 6. I-V measurements of steady-state conductance in 20-nm-thick $Al_{0.72}Sc_{0.28}N$ capacitors during various switching stages. (A) PFM images of the domain structures at each switching stage with a fixed poling voltage of 13 V. (B) Corresponding I-V characteristics. (C and D) Estimated polarization switching fractions (percentage of domains in the upward state) (C), and corresponding leakage currents at 4 V (D) for each switching stage[70].

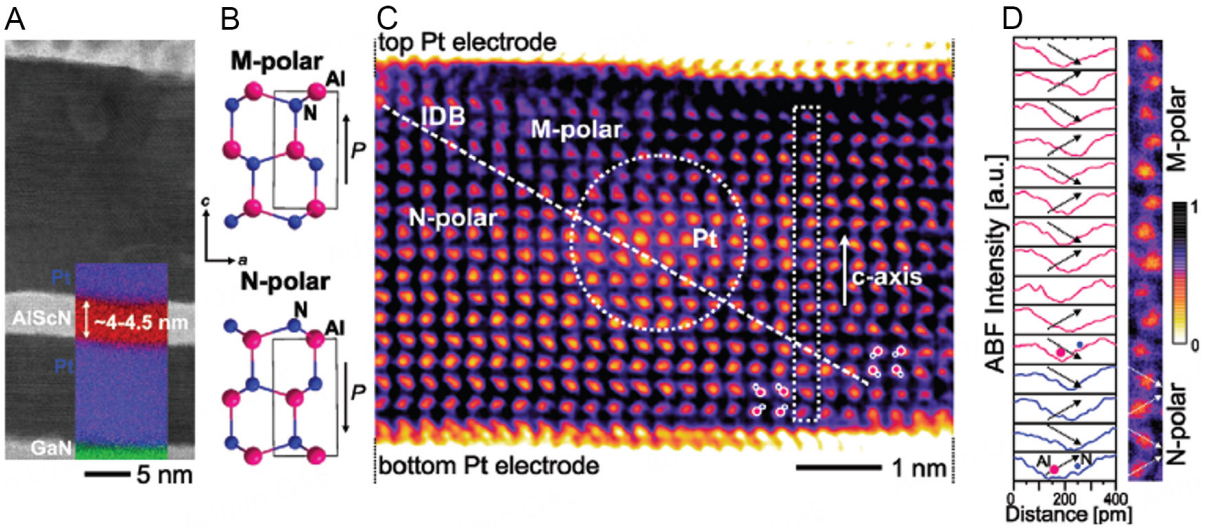

Figure 7. ABF-STEM micrograph showing the Pt/$Al_{0.74}Sc_{0.26}N$/Pt/GaN capacitor stack in cross-section. (A) The inset shows superimposed EDS maps of Pt, Al, and Ga. (B) Atomic structure sketches of M- and N-polar states. (C) Inverted ABF-STEM micrograph sketches of an inclined inversion domain boundary separating M-polar (upper right) and N-polar (lower left) regions, with overlaid (Al,Sc)-N dumbbell schematics indicating polarization direction. (D) Intensity profiles of polarization direction within individual (Al,Sc)-N dumbbells, with arrows indicating profile direction and color-coded polarity: M-polarity = pink, N-polarity = blue[6].

One key challenge for advancing and enabling mass production of efficient devices is understanding the origin of ferroelectricity in the wurtzite structure. Two main perspectives are considered: (1) local chemical effects involving structural instabilities; and (2) extended structural effects such as lattice flattening. However, the origin remains incompletely understood. The main hypotheses include:

• Local chemical effects: Ferroelectric behavior arises from atomic-level instabilities caused by defects (e.g., vacancies or interstitials) or substitutional disorder. Sc doping introduces bond frustration between tetrahedral Al^{3+} and octahedral Sc^{3+} coordination, disrupting the sp^3 covalent network and lowering polarization stability.

• Structural modification: Ferroelectricity may also be linked to the arrangement of atomic layers, particularly under high defect concentrations or external stress. Global lattice flattening (reduced c/a ratio) enables polarization rotation via a metastable hexagonal (H) phase. However, DFT calculations show that this contributes < 15% to the overall switching energy reduction, with local bond ionicity playing a more dominant role.

A synergistic mechanism is likely: local Sc-N ionic bonding reduces the intrinsic energy barrier for polarization rotation, while structural flattening (reduced c/a ratio) stabilizes intermediate states, enhancing ferroelectric switching (e.g., through the H-phase). Isolating local and global structural effects remains difficult, as traditional tools like X-ray diffraction (XRD) and PFM provide only averaged material properties. Advanced 4D-STEM now enables mapping of polarization vectors at atomic resolution, revealing domain wall pinning at Sc-rich clusters. Another challenge lies in the strong sensitivity of wurtzite ferroelectricity to composition and growth conditions, complicating reproducibility and hindering comprehensive understanding. Despite this, significant progress has been made through advanced tools such as scanning transmission electron microscopy (STEM) and atom probe tomography, which enable detailed characterization of local structures. For instance, 4D-STEM can resolve transient H-phase domains during switching by tracking lattice parameter evolution at nanosecond timescales. A deeper understanding

of these mechanisms will facilitate the design of new materials with optimized ferroelectric properties, supporting the development of next-generation devices.

Impact of scandium concentration on lattice parameters

The evolution of lattice parameters in $Al_{1-x}Sc_xN$ thin films reflects a complex interplay between Sc-induced strain and phase stability. Satoh *et al.*[74] studied structural deformation and phase transitions in $Al_{1-x}Sc_xN$ as Sc content varied from 0 % (AlN) to 100% (ScN). The wurtzite phase remains stable up to x = 0.3. Between x = 0.3 and 0.35, a two-phase mixture emerges, comprising both wurtzite and cubic structures. This coexistence is due to competing coordination preferences: Al^{3+} stabilizes tetrahedral sp^3 bonding, while Sc^{3+} favors octahedral sd^3 hybridization, resulting in nanoscale strain mosaics. The complete transition to a cubic phase occurs between x = 0.38-0.43. During this evolution, a significant decrease in the c-axis lattice parameter is observed as Sc increases from 0.16 to 0.35, indicating a transition from the B4-type wurtzite structure to the B1-type rocksalt structure. At x = 0.38, the c-axis parameter unexpectedly increases - likely due to cubic phase nucleation relieving c-axis strain in residual wurtzite domains [Figure 8]. This trend is consistent with findings by Petrich *et al.*[75], who also observed initial lattice expansion followed by contraction at higher Sc contents.

Lu *et al.* further linked these structural changes to switching dynamics[70], showing that reduced c/a ratios at x = 0.28 decrease steric hindrance for polarization rotation, enabling domain wall velocities > 1 m/s under fields > 6 MV/cm. This interplay between lattice flattening and Sc-N bonding underpins Sc's dual role in enhancing both piezoelectric and ferroelectric properties.

This analysis highlights the substrate's significant role in the evolution of lattice parameters. Both studies, anchored in experimental data, reveal similar trends; however, Satoh *et al.* specifically observed a notable decrease in the *c*-axis lattice parameter with increasing Sc content when the films were deposited on sapphire substrates[74]. This effect is attributed to sapphire-induced biaxial tensile strain, which promotes basal plane expansion and amplifies the lattice-distorting influence of Sc. These findings underscore the importance of substrate effects on lattice dynamics. The observed changes likely result from localized interactions between Sc and Al atoms in the lattice. In the mixed-phase region, the Sc concentration is higher in the cubic phase than in the wurtzite phase, leading to a relief of c-axis distortion in residual wurtzite domains once the Sc ratio exceeds 0.35. This phase segregation occurs because of Sc^{3+}'s preference for octahedral coordination, driving its incorporation into the cubic phase. At lower Sc content (x = 0 to 0.16), substitution into Al sites introduces lattice strain and distortion, causing expansion along the <110> direction and increasing both a and c lattice constants. Initially, this trend follows Vegard's law, but above x = 0.2, deviations occur due to bond frustration[76].

Substrate and strain effects

Substrate-induced strain, interfacial interactions, and growth templating critically influence lattice parameters and phase stability in thin films. Substrate engineering is key to stabilizing metastable wurtzite phases, minimizing defects, and optimizing ferroelectric performance. For instance, Zheng *et al.*[7] employed c-axis sapphire substrates with epitaxial <111>Al bottom electrodes to grow highly oriented $Al_{0.72}Sc_{0.28}N$ films. The high thermal boundary conductance of Al/sapphire suppressed hillock formation during 350 °C deposition, yielding smooth, defect-free Al layers[77]. Cross-sectional TEM confirmed sharp Al/AlScN interfaces, crucial for minimizing leakage currents in sub-10 nm films. In contrast, Si-based substrates suffer from lattice mismatch and interfacial oxide formation, degrading ferroelectric performance[70]. Strain effects differ by substrate: silicon induces compressive strain that stabilizes the wurtzite phase up to x = 0.35, while sapphire substrates impose biaxial tensile strain, amplifying basal plane expansion[74,75]. Zheng *et al.*

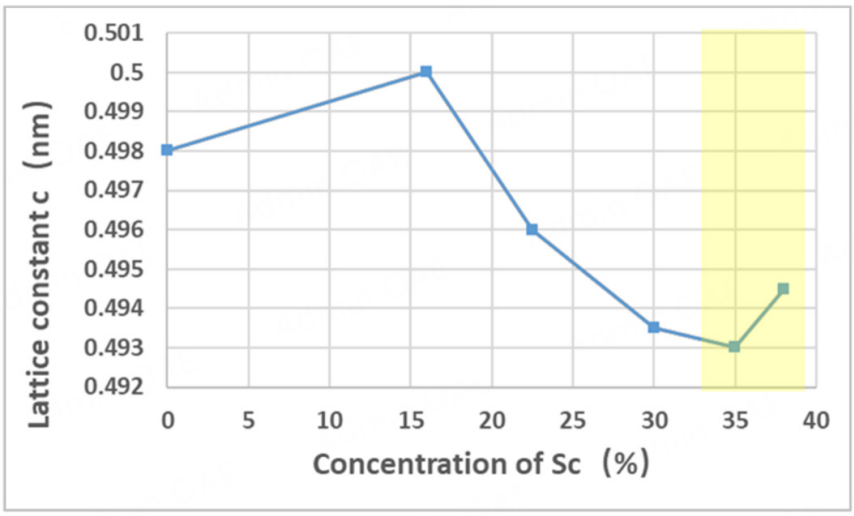

Figure 8. Dependence of the c-axis lattice constant on Sc concentration in $Al_{1-x}Sc_xN$. The two-phase coexistence region is highlighted in yellow. Adapted from Ref.[74].

demonstrated that Al template-induced in-plane compressive strain on sapphire yields out-of-plane tensile strain in AlScN, increasing the c-axis lattice parameter from 5.01 Å (27 nm film) to 5.07 Å (5.4 nm film)[7]. Strain engineering also mitigates premature capacitor breakdown, a common issue in polycrystalline films on Pt or Si. Satoh *et al.*[74] observed a decrease in the c-axis lattice constant at higher Sc ratios on sapphire, suggesting localized substrate interactions.

Seed layers and buffer materials further expand the scope of substrate engineering strategies. Saha *et al.*[28] reported a phase transition from the wurtzite to a mixed phase at Sc concentration of 0.28, and demonstrated the stabilization of cubic AlScN ($0.62 \leq x \leq 0.82$) using a TiN buffer layer on MgO. The TiN lattice (≈ 4.24 Å) acts as a template for cubic AlScN, reducing interfacial energy. This stabilization is critical, as it enables the growth of $Al_{1-x}Sc_xN$ films with a wurtzite structure even at high scandium concentrations. Momida *et al.*[40] found that their DFT results aligned well with experimental c-axis trends up to Sc = 0.2, but diverged at higher concentrations ($x > 0.5$), where DFT underestimates bond frustration in the solid solution. Seed layers also critically influence phase integrity. Höglund *et al.*[54] showed that ScN seed layers promote cubic symmetry up to 60% Sc, while AlN seed layers preserve the wurtzite phase up to Sc = 0.48. These interactions may influence the piezoelectric response more significantly than lattice changes alone. In addition to phase stabilization, seed layers enable control over film polarity. Growth mechanisms further affect polarity: Milyutin *et al.*[78] achieved Al-polarity in sputter-deposited AlN using MOCVD seed layers, which favor layer-by-layer growth (75% Al termination) over stochastic sputtering. Similarly, Zheng *et al.*[7] demonstrated that epitaxial Al electrodes act as effective growth templates, minimizing defects and interfacial charge traps - crucial for reliable performance in sub-10 nm ferroelectric devices.

A landmark study by Yasuoka *et al.*[79] established a connection between substrate-induced strain and crystal anisotropy. By depositing $Al_{0.8}Sc_{0.2}N$ films on fused silica, Si, Al_2O_3, and MgO substrates with varying thermal expansion coefficients α_{sub}, they systematically modulated in-plane tensile or compressive strains during cooling from 400 °C. X-ray diffraction analysis revealed that increasing α_{sub} reduced the anisotropy parameter u (calculated as $u = a^2/3c^2 + 1/4$), which quantifies structural distortion in the wurtzite lattice. Ferroelectric hysteresis measurements showed that coercive field increased with α_{sub}, while the remanent polarization decreased linearly with u. For instance, films on fused silica ($\alpha_{sub} = 0.54 \times 10^{-6}$ °C) exhibited

u = 0.382 and E_c = 4.2 MV/cm, whereas films on MgO (α_{sub} = 13 × 10^{-6} °C) showed u = 0.377 and E_c =5.8 MV/cm. This study bridges structural anisotropy and functional properties, highlighting that substrate selection enables precise tuning of P_r and E_c without altering the Sc concentration. These findings align with theoretical models by Dreyer *et al.*[73] and Furuta *et al.*[69], which predict P_r dependence on u and underscore the combined roles of chemical doping, strain engineering, and interfacial templating in optimizing wurtzite ferroelectrics.

Phase transitions and structural evolution

Research indicates that polarization switching may occur via an intermediate H-phase transition - a theorized metastable hexagonal phase positioned between the M-polar and N-polar states, as illustrated in Figure 9. This pathway has been predicted computationally (e.g., through Berry phase simulations by Dreyer *et al.*[73]), but direct experimental observation remains elusive. Detecting such a transient state would require non-equilibrium techniques such as ultrafast cryogenic TEM to capture short-lived configurations or strain engineering with piezoelectric substrates to stabilize the hexagonal structure. In the proposed H-phase, Al atoms occupy positions within the plane of N atoms, forming an artificial configuration, as noted by Dreyer *et al.*[73]. The H-phase is hypothesized to act as a nonpolar transition state (u ≈ 0.45), where N^{3-} planes lead the $(Al,Sc)^{3+}$ planes by ~0.5 Å, and the associated activation energy is only 0.3 eV/unit cell at x = 0.5. This hexagonal phase was used as a zero-polarization reference in Berry phase simulations, yet its role in switching dynamics remains theoretical and requires empirical validation. The structural behavior of $Al_{1-x}Sc_xN$ shows that buckling decreases in the M-polar phase and increases in the N-polar phase, with the H-phase proposed to mediate this transformation. Computational studies on AlN and ScN - such as the work by Farrer *et al.*[80], who predicted the existence of a metastable hexagonal ScN with nearly fivefold coordination using local-density approximation (LDA) - support the existence of such a phase, reinforcing the hypothesis that polarization switching in wurtzite $Al_{1-x}Sc_xN$ may proceed via the H-phase. Although the equilibrium structure remains wurtzite, it is hypothesized that atomic rearrangements into a hexagonal configuration occur during switching, though this has yet to be observed.

Importantly, the H-phase transition has not been experimentally demonstrated in AlN. Thermodynamic analyses indicate a significant energy barrier to achieving this phase under equilibrium conditions. To validate this hypothesis, non-equilibrium deposition methods such as molecular beam epitaxy or pulsed laser deposition under high strain could potentially stabilize the H-phase. *In situ* techniques - such as TEM under applied electric fields or synchrotron X-ray diffraction during polarization switching - could directly capture transient hexagonal intermediates. Additionally, ultrafast spectroscopy (e.g., pump-probe XRD) might be employed to detect short-lived H-phase states during switching. Findings by Zhang *et al.*[52] report a marked reduction in the c/a ratio within the Sc concentration range of 0.5 to 0.625, corresponding to an increase in the u parameter. At x = 0.5625, the c/a ratio stabilizes near 1.35, while u approaches 0.45. Within this compositional window, the hexagonal phase exhibits enhanced thermodynamic stability compared to rocksalt structures. This stability is attributed to partial ionic screening, where Sc 3d electrons hybridize with N 2p orbitals, lowering the system's energy. However, as the composition increases beyond x ≥ 0.625 - approaching h-BN-like characteristics with u ≈ 0.5 - the energetic preference shifts back toward the rocksalt phase. While the polar-to-nonpolar phase transition in this regime remains speculative, theoretical predictions suggest that h-BN-like ScN could exhibit ferroelectricity under (0001)-oriented strain. Nonetheless, two key challenges hinder the synthesis of metastable h-BN ScN. First, its formation energy (~0.32 eV per formula unit) is significantly higher than that of the stable rocksalt phase. Second, its realization would require considerable in-plane strain (3%-7%), adding strain energy costs of approximately 0.08-0.21 eV per formula unit. This combination renders the h-BN phase unstable and difficult to achieve in practice. Consequently, for Sc concentrations above x = 0.625, the energetically preferred structure reverts to

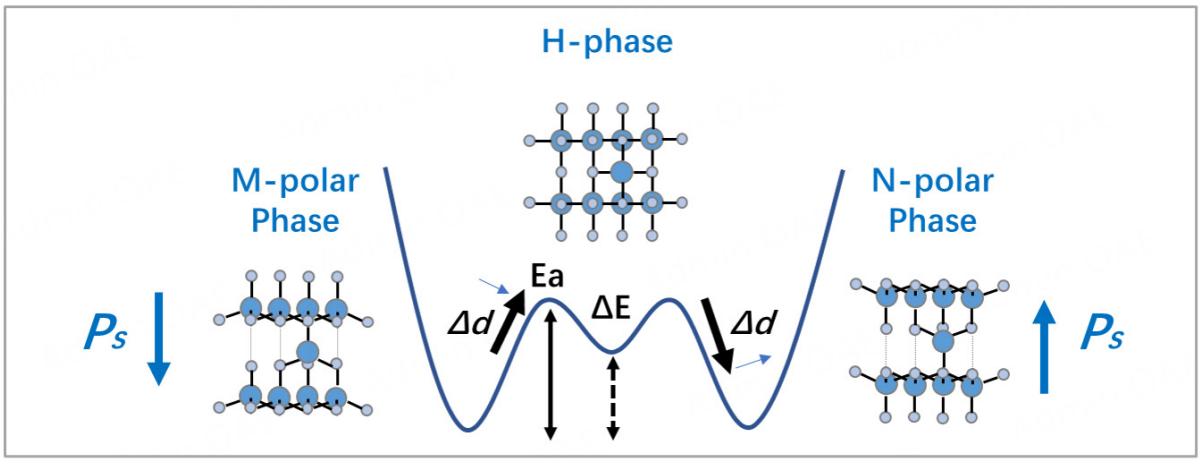

Figure 9. Schematic energy landscape of AlN during the polarization switching via the H-phase transition[30].

the rocksalt phase, underscoring the complex relationship between composition and phase stability in Sc-based nitrides.

In $(AlN)_n/(ScN)_m$ superlattices (SLs), increasing the ScN fraction (x) to 0.5 results in anisotropic lattice expansion: the lattice constants a_{SL} and c_{SL} increase by 5.8% and 5.5% respectively, due to interface strain[30]. In contrast, the solid solution (SS) displays a less consistent trend - c_{SS} shows no monotonic change with x, while a_{SS} increases more significantly, by 7.6% at x = 0.5. The nearly constant c/a ratio in the SL, compared to its decrease in the SS, suggests that strain gradients in the SL may help stabilize the H-phase. Experimental validation using cross-sectional TEM combined with atomic-scale EELS/EDS mapping could resolve local strain fields and hexagonal motifs.

Reconciling structural flattening and Sc-N bonding perspectives

The ferroelectric switching barrier (Ea) shows a significant reduction with increasing x. Specifically, Ea decreases by 66% for SL, while only by 5% for SS, compared to AlN at x = 0.5. This stark contrast suggests that interface-driven strain gradients in SLs, rather than bulk compositional changes in SS, are critical for H-phase stabilization. Therefore, the reduction in Ea cannot be solely attributed to atomic structure flattening. The coordination instability associated with ScN in the wurtzite structure must also be factored in, as it indicates localized structural instability. In contrast, the rocksalt phase of ScN represents a more stable configuration due to its octahedral bonding, while wurtzite ScN remains inherently unstable. This instability is critical in narrowing the energy gap between the wurtzite and hexagonal phases, thereby lowering the switching barrier, since polarization switching proceeds via the H-phase transition. This study emphasizes a crucial reduction in activation energy (E_a) linked to structural instability in both SL and SS systems. Analysis of the energy difference (ΔE) between the wurtzite and hexagonal phases of $Al_{1-x}M_xN$ reveals a dependence on the dopant M, which becomes particularly pronounced at higher concentrations. These findings underscore the importance of selecting a dopant with an inherently unstable wurtzite structure, as this effectively lowers both ΔE and Ea in Wurtzite-(Al, M)N systems. Moreover, for M = Sc, spontaneous polarization decreases markedly with increasing x.

Yazawa *et al.* provide a key perspective, emphasizing the role of Sc-N chemical bond dynamics over simplistic structural flattening arguments (i.e., changes in the c/a ratio)[81]. Their electron localization function (ELF) analysis demonstrates that Sc doping reduces charge localization at Al-N bonds, facilitating

easier dipole reorientation. This behavior results from a transition from covalent Al-N bonding - dominated by directional sp^3 hybridization - to more ionic, non-directional Sc-N interactions involving sd^3 hybridization. The increased bond ionicity at higher Sc concentrations lowers the Peierls-Nabarro barrier for domain wall motion, facilitating polarization reversal. DFT calculations further reveal that Sc substitution contracts in-plane Al-N bonds by 0.05 Å while elongating out-of-plane bonds by 0.12 Å. This distortion creates local h-BN-like motifs that act as nucleation sites for polarization reversal. Yazawa's work shows that even at low Sc concentrations (observed across a range of compositions, $0 < x < 0.35$, and thicknesses of 140-260 nm), the local chemical environment - particularly the ionic character of Sc-N bonds - dictates the energy landscape for switching, independent of global lattice parameter trends. Combinatorial thin films of $Al_{1-x}Sc_xN$ demonstrate a significant reduction in both the coercive field and spontaneous polarization as Sc content increases. This trend mirrors that observed in homogeneous films, where variations in the c/a ratio correlate with changes in the Sc ratio. A pure wurtzite phase is retained for Sc concentrations below 0.35, while a mixed phase emerges beyond this threshold. This transition from a pure wurtzite to a mixed phase aligns with the findings of Satoh *et al.*[74]. However, the variation in lattice parameters observed here indicates a more invariant c/a ratio with composition than previously reported. These changes in lattice parameters - and the Sc concentrations at which phase transitions occur - are influenced by factors such as the choice of seed layers and underlying metal layers. Such effects can be attributed to stochastic interactions within the Al-Sc subsystem of the broader Al-Sc-N system. Ultimately, the system's dynamics are governed by interactions between the dopant and host atoms. Notably, changes in the Al-Sc system with increasing Sc concentrations show parallel trends in alloy lattice parameters, particularly the c lattice parameter [Table 1 and Figure 10], consistent with the observations of Satoh *et al.*[74] and Petrich *et al.*[75]

While earlier studies by Akiyama *et al.*[60] and others attributed polarization switching primarily to macroscopic structural flattening (i.e., a reduction in the c/a ratio), Yazawa's findings complicate this narrative by highlighting the dominant role of local chemical interactions. However, these perspectives are not mutually exclusive. Structural flattening provides a macroscopic framework for understanding phase stability and lattice distortion, which creates favorable conditions for switching. In parallel, Yazawa's work underscores that the ionic nature of Sc-N bonds governs the microscopic energy barriers for domain wall motion. This distinction is approximately reflected in their relevance across different Sc concentrations:

• At low Sc concentration ($x < 0.2$): Local chemical effects dominate. Isolated Sc atoms disrupt the covalent Al-N network, introducing bond frustration and localized ionic regions that lower the energy barrier for switching.

• At intermediate concentrations ($0.2 < x < 0.4$): Both mechanisms coexist. Structural flattening (c/a reduction) softens the lattice globally, while Sc-N ionic bonds reduce local switching barriers.

• At high concentration ($x > 0.4$): Phase segregation and cubic phase nucleation destabilize ferroelectricity, rendering both mechanisms less effective.

Thus, Yazawa's work does not contradict earlier structural models but rather complements them by revealing atomic-scale drivers of switching that act alongside macroscopic lattice effects. This dual-scale understanding is essential for optimizing the ferroelectric performance of AlScN, as it suggests that both compositional tuning (to enhance bond ionicity) and strain engineering (to control the c/a ratio) are necessary for effective device design.

Table 1. Al-Sc lattice parameter data

Phase	Composition (at. % Sc)	Lattice constant a (nm)	Reference
Al	0	0.40496	[82]
Al_3Sc	25	0.4103	[83]
Al_2Sc	33.3	0.7582	[84]
AlSc	50	0.3450	[85]
$AlSc_2$	66.7	0.4888	[86]

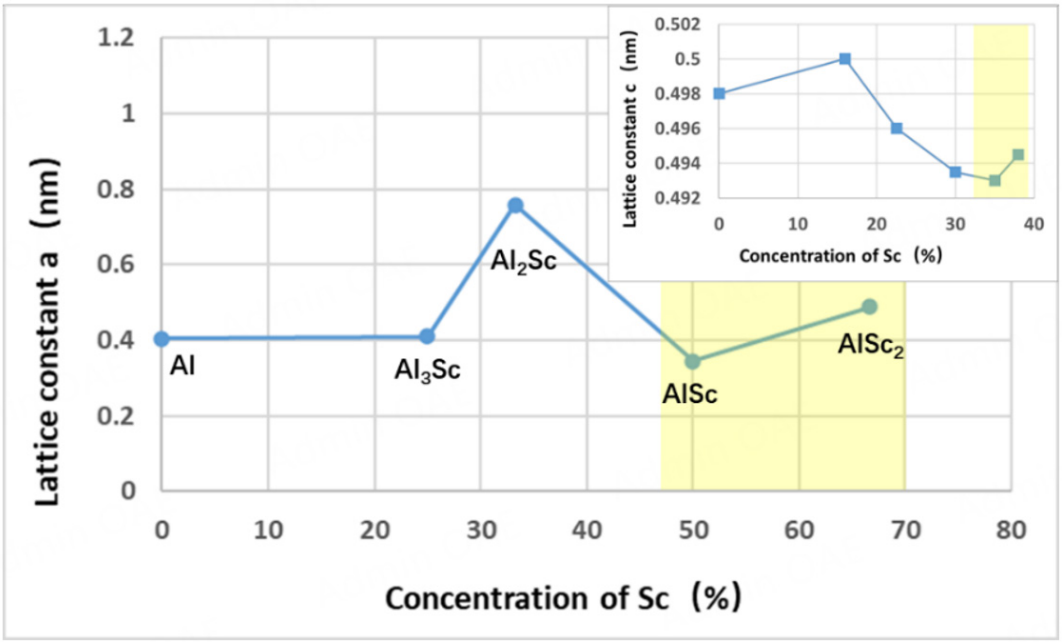

Figure 10. Sc concentration dependence of the lattice constant a in the Sc-Al Structure. A similar variation in parameter a is observed, consistent with trends in the c lattice parameter of the $Al_{1-x}Sc_xN$ structure.

The origin of ferroelectric behavior in wurtzite structures likely stems from a combination of local chemical and structural effects. Atomic-scale studies of the Al-B-N system highlight the role of transient non-polar configurations in mediating polarization reversal[23]. DFT calculations show that boron doping flattens the energy landscape, enabling the wurtzite lattice to access a metastable antipolar state during switching [Figure 11].

This intermediate state, characterized by alternating N-polar and Al-polar motifs, resembles inversion domain boundaries observed in non-ferroelectric III-nitrides[87,88]. Real-time DPC-STEM imaging further supports this mechanism, revealing that switching initiates at localized nucleation sites and propagates via domain wall motion. These findings bridge local chemical effects (bond distortion) with global structural dynamics (domain propagation), offering a unified model for ferroelectricity in wurtzite materials. This duality underscores the importance of optimizing doping strategies to balance ionic character (to lower intrinsic energy barriers) and structural flexibility (to accommodate transient states), as exemplified by emerging $Al_{1-x}(Sc,B)_xN$ quaternary alloys.

Studies by Skidmore *et al.*[4] on heterostructures further highlight the role of interfacial strain and electric fields in facilitating switching. DFT calculations indicate that biaxial tensile strain reduces the polarization

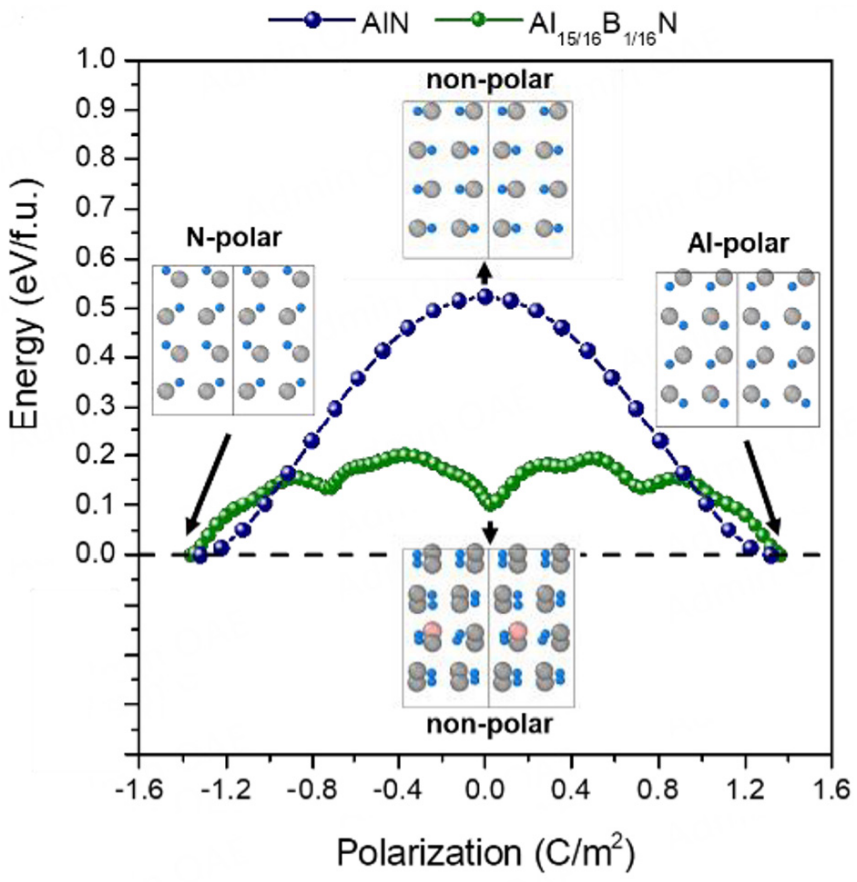

Figure 11. Nudged-elastic-band simulation of polarization reversal pathways for AlN and $Al_{15/16}B_{1/16}N$. The insets show structural models at specific simulation stages[23].

reversal barrier in AlN by ~ 15%, consistent with prior work on strain-mediated polymorph stabilization in wurtzite structures[23]. Their proposed model suggests that charged domain walls in the ferroelectric layer generate unscreened electric fields (> 100 MV/cm) and elastic distortions at the interface, which transiently destabilize the non-ferroelectric lattice into a metastable, switchable state [Figure 12][22,23].

These results align with observations in AlN/AlScN heterostructures, where interfacial domain propagation enables collective switching without chemical substitution[22]. This mechanism is reminiscent of behavior in perovskite heterostructures, where interfacial electric fields modulate polarization[89], but differs by leveraging the low permittivity of nitrides to sustain high field concentrations without dielectric breakdown.

Polarization switching mechanisms

The polarization switching mechanism in $Al_{1-x}Sc_xN$ involves a nuanced interplay between structural evolution and local chemical bonding. While earlier studies attributed the reduced switching barrier primarily to structural flattening (i.e., a reduction in the c/a ratio), recent analyses reveal that the nature of Sc-N chemical bonds plays an equally critical role. This dual influence - structural and electronic - creates a multi-scale mechanism, wherein macroscopic lattice distortions enable polarization reversal, while localized ionic bonding at Sc sites governs the energy landscape of the switching process. Direct evidence of this synergy is provided by *in situ* STEM imaging of $Al_{0.94}B_{0.06}N$, where polarization reversal is mediated by a transient non-polar state [Figure 5A].

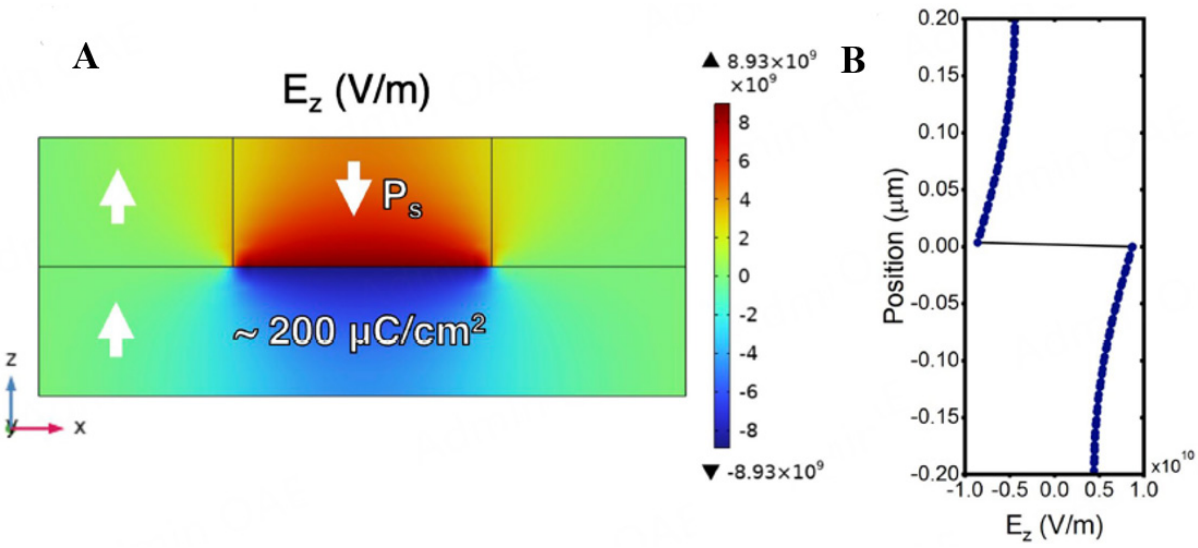

Figure 12. (A) COMSOL simulation of electric field distribution along the z-direction in a ferroelectric slab with a head-to-head domain wall perpendicular to the polar axis, assuming a remanent polarization of 100 μC/cm^2. The field concentrates at the wall. (B) Line scan at the center of the domain wall shows a peak electric field of 100 MV/cm, assuming full polarization is maintained to the wall edge[4].

Ye *et al.*[30], using *ab initio* calculations, propose that local structural instabilities induced by Sc doping dominate over bulk lattice flattening in reducing the switching barrier. Their findings align with experimental observations showing that the reduction in coercive field correlates more strongly with Sc-N bond ionicity than with trends in the c/a ratio. For instance, at x = 0.25 Sc, the c/a ratio remains nearly unchanged, yet E_c decreases by ~40%, suggesting that bond-level effects drive the switching dynamics even before significant structural flattening occurs. The transient non-polar state observed in Al-B-N systems mirrors the hypothesized H-phase pathway in Al-Sc-N, suggesting a potentially universal switching mechanism in wurtzite ferroelectrics [Figure 5B]. Further support comes from Keisuke Yazawa's ELF analysis, which demonstrates that Sc substitution disrupts the sp^3 hybridization of Al-N bonds and replaces them with non-directional ionic Sc-N interactions[81]. These weaker directional constraints reduce the energy required for bond reorientation during polarization reversal, even in the absence of pronounced lattice flattening. This transition from covalent to ionic bonding reduces the Peierls-Nabarro barrier for domain wall motion, facilitating polarization reversal. However, structural flattening remains relevant at higher Sc concentrations (x > 0.3), where Sc-induced lattice expansion lowers the energy barrier between polarization states. DFT calculations reveal significant differences in Al-N and Sc-N bond lengths, attributed to the disparity in ionic radii between Al and Sc, as well as the unfavorable tetrahedral coordination of Sc^{3+}. Even at low concentrations, Sc substitution exerts localized effects on Al-N bond lengths - contracting basal-plane bonds while elongating out-of-plane bonds. These changes are consistent with a local structure approaching the 6/mmm hBN-like symmetry, indicative of a non-polar intermediate state during switching in the wurtzite ferroelectric system[46,34]. Accordingly, Sc doping produces two simultaneous effects: (1) local ionic bonding reduces the covalent stiffness of the lattice, facilitating easier bond rotation; and (2) extended lattice distortion - manifested as an increased u parameter and basal plane expansion - stabilizes intermediate states such as the hypothetical H-phase.

These processes are synergistic rather than contradictory. At low concentrations (x < 0.2), ionic bonding dominates the switching mechanism, as evidenced by ELF maps showing isotropic charge distributions around Sc atoms even in minimally distorted lattices[81]. At higher concentrations (x > 0.3), structural flattening further amplifies the effect by reducing steric hindrance to polarization rotation. This explains the

nonlinear acceleration of E_c reduction with increasing Sc content: bond ionicity establishes the foundational mechanism, while lattice distortion further lowers the activation energy.

The role of the H-phase transition exemplifies this synergy. While structural flattening (c/a ~ 1.35) theoretically stabilizes the H-phase, successful switching through this pathway depends critically on the Sc-N bond's ability to accommodate metastable hexagonal coordination - a property absent in pure AlN due to its rigid covalent network. DFT studies confirm that Sc-doped systems exhibit smaller energy differences ($\Delta E < 0.1$ eV/atom) between wurtzite and H-phase configurations compared to pure AlN ($\Delta E > 0.5$ eV/atom)[73]. Thus, the dual impact of Sc doping - weakening directional bonding and distorting the lattice - makes the H-phase pathway accessible. This framework helps reconcile previously conflicting interpretations: while structural flattening (c/a reduction) provides a necessary but insufficient condition for low-E_c switching, Sc-N bond ionicity serves as the enabling factor by lowering the intrinsic energy barrier for polarization rotation. Supporting this model, combinatorial studies show that coercive fields correlate more strongly with Sc-N bond ionicity (measured via XPS binding energy shifts) than with c/a ratios over the range $0.2 < x < 0.4$[90]. Similarly, epitaxial strain experiments demonstrate that tensile strain alone cannot reduce E_c in undoped AlN below 4 MV/cm, whereas Sc-doped films ($x = 0.3$) achieve E_c ~2.5 MV/cm under identical strain conditions[80]. These findings confirm that ionic bonding - rather than lattice geometry alone - is essential for practical ferroelectric switching.

Thickness-dependent ferroelectric properties

Thickness scaling is critical for integrating $Al_{1-x}Sc_xN$ into CMOS-compatible devices. Recent breakthroughs in sputter-deposited $Al_{0.72}Sc_{0.28}N$ films have demonstrated robust ferroelectricity at thickness as low as 5.4 nm - a milestone previously unachieved in sputtered systems. Zheng *et al.*[7] systematically studied films ranging from 27.1 to 5.4 nm, revealing a thickness-dependent increase in the normalized coercive field, from 4.4 MV/cm at 27.1 nm to 7.3 MV/cm at 5.4 nm under 10 KHz excitation. Simultaneously, the breakdown field of capacitors with a 12.5 μm radius improved from 8.3 to 12.1 MV/cm, highlighting the defect-limited nature of breakdown in thinner films. Remarkably, the 5.4 nm film achieved full ferroelectric switching at 5.5 V (10.2 MV/cm) under 500 ns pulses, with a switching speed of 60 ns - critical for low-voltage, non-volatile memory applications. The high c-axis orientation (XRD rocking curve FWHM: 3.52°-4.44°) and minimal interfacial layers in these ultrathin films underscore the effectiveness of Al/sapphire templates in mitigating strain relaxation and suppressing hillock formation. These advancements contrast with MBE-grown AlScN films, which, while achieving similar thickness, face significant scalability challenges[91]. Recent advances in ultrathin $Al_{1-x}SC_xN$ films have further demonstrated the potential to reduce switching voltages without compromising ferroelectric performance. Schönweger *et al.*[6] achieved a major breakthrough by sputter-depositing sub-5 nm $Al_{0.74}Sc_{0.26}N$ films on Pt/Ti/SiO_2/Si substrates, realizing coercive voltages as low as 1 V - compatible with standard on-chip voltage supplies. This represents a 50% reduction in switching voltage compared to prior reports of 5 nm MBE-grown epitaxial films[91] and 10 nm sputtered AlScN on Si[92]. The study uncovered a unique thickness-dependent coercive field scaling trend: while E_c increased slightly as thickness decreased to 10 nm, it dropped sharply below 10 nm, reaching < 2 MV/cm for 4-4.5 nm films. This deviation from the classical Janovrc-Kay-Dunn scaling was attributed to depolarization field effects exacerbated by finite electrode screening lengths, consistent with models proposed by Dawber *et al.*[31]. The Dawber model attributes field enhancement at the electrodes to finite screening lengths, which amplify the applied field when $4 \Pi Ps > > \varepsilon_0 \varepsilon_r E$, introducing a correction factor into the Janovec-Kay-Dump framework[31,93]. First-principles calculations also suggest that non-switchable wurtzite III-V materials develop depolarization fields that scale inversely with film thickness (1/d)[94].

Divergent thickness-dependent E_c trends have emerged across different growth methods and interfacial conditions. The coercive field and remnant polarization of $Al_{1-x}Sc_xN$ exhibit thickness-dependent behavior that is strongly influenced by interfacial chemistry and strain states. Wang *et al.*[91] systematically investigated the thickness scaling of MBE-grown $Al_{0.7}Sc_{0.3}N$ films on Mo (011), revealing anomalous E_c behavior in ultrathin layers (5-100 nm). Although classical models predict $E_c \propto d^{-2/3}$, E_c increased disproportionately in the 5 nm film due to two main factors:

• Surface oxidation: A 1 nm native oxide layer formed post-growth introduced trapped charges that pinned polarization.

• Compressive strain: Epitaxial mismatch with the Mo substrate induced in-plane compressive strain, distorting the wurtzite lattice and raising the energy barrier for switching.

Notably, the oxide layer modulated the interfacial energy barrier, enabling robust ON/OFF ratios ($> 10^3$) and retention even with a reduced remnant polarization ($P_r \sim 23$ μC/cm^2) in 5 nm films.

This behavior stands in stark contrast to that observed by Schönweger *et al.*[6], where the native oxide on Si acted as a charge reservoir, enabling low-voltage switching and resulting in a reduced E_a in sub-5 nm $Al_{0.74}Sc_{0.26}N$ films.

Key mechanistic distinctions

Wang *et al.*[91] (oxide/ferroelectric interface): Trapped charges at the oxide interface amplified polarization pinning, overriding the expected thickness-dependent decrease in E_c.

• Schönweger *et al.*[6] (ferroelectric/Si interface): The native oxide layer compensated depolarization fields, allowing E_c to scale inversely with thickness.

• Zheng *et al.*[7] (sputtered films): Tensile strain due to lattice mismatch was the dominant factor affecting switching behavior with decreasing thickness.

Furthermore, Schönweger *et al.*[6] reported a thickness-dependent increase in relative permittivity (ε_r), rising from ~ 14 in 100 nm to ~ 18 in sub-5 nm films. This was attributed to domain wall proliferation during electrical cycling. The study underscored the critical role of substrate-induced strain in modulating ferroelectric properties - specifically, the thermal tensile strain on Si substrates ($\varepsilon_{thermal} \approx 0.09\%$) *vs.* the compressive strain observed on sapphire - reinforcing mechanisms previously documented in strained AlScN films[73].

Local coordination and chemical bonding analysis

A significant study by Cohen *et al.* elucidates the local configurational environment of dopant elements (Sc or Y) in AlN films[14]. In the interaction between nitrogen and aluminum, the 2s and 2p orbitals of N hybridize with the 3s and 3p orbitals of Al, resulting in sp^3 hybridization and establishing a tetrahedral coordination typical of the hexagonal wurtzite structure. In contrast, Sc interacts with N through its 3d and 4s orbitals, facilitating octahedral coordination characteristic of the cubic rocksalt structure. The 3d electrons of Sc participate in sd^3 hybridization with the 2p orbitals of N, lowering the energy of octahedral sites relative to tetrahedral ones. When aluminum nitride is alloyed with scandium nitride, a strong competition arises between their distinct bonding geometries: tetrahedral Al-N bonds favor sp^3

hybridization, while octahedral Sc-N bonds involve sd-sp interactions. These contrasting coordination preferences between the tetrahedral AlN phase and the octahedral ScN phase are pivotal to the structural characteristics of $Al_{1-x}Sc_xN$ alloys. Experimental studies investigating varying Sc content (specifically at x = 0.25 and 0.30) reveal significant structural changes, as supported by EXAFS analysis[14]. This analysis showed a shift in coordination number from 4 at x = 0.25 to 6 at x = 0.3, indicating an evolving structural dynamic as scandium concentration increases. At x = 0.30, the EXAFS Debye-Waller factor increased by 0.02 $Å^2$, confirming bond disorder due to mixed coordination environments. This suggests that a fraction of Sc ions undergo a transition from tetrahedral to octahedral coordination, even at Sc concentrations below the critical threshold of approximately x = 0.42 associated with the wurtzite-to-rocksalt phase transition. These findings align with the ELF analysis conducted by Yazawa *et al.*[81] at x = 0.25. Their results showed high ELF values around Al-N bonds, indicative of directional polar covalent bonding dominated by sp^3 hybridization. In contrast, the ELF distribution around Sc atoms was more isotropic, reflecting a delocalized electron distribution characteristic of ionic bonding. Furthermore, Fichtner *et al.*[46] reported an absence of observable ferroelectric switching at Sc concentrations below x = 0.22, with measurements beginning at x = 0.27. This raises the question of whether lattice parameter variation alone is the primary mechanism driving ferroelectric behavior in the wurtzite structure. In the following section, we explore the effects of other dopant elements within the wurtzite framework and their influence on polarization and ferroelectric properties.

Metal-doped AlN

As previously discussed, the ferroelectric properties of the material are influenced by local structural interactions, specifically the atomic interactions governed by the ratio of the doping metal. This enhancement in switchability has significant implications for non-volatile memory technologies. In this section, we examine the effects of metal doping on AlN and other wurtzite-structured materials in the context of polarization switching.

Polarization switching is based on the potential for polarity inversion - a critical feature that can determine the switching mechanism. Understanding the polarization inversion process is therefore essential for revealing the underlying phenomena. Anggraini *et al.*[15] demonstrated that doping AlN with Si and MgSi facilitates a transition from Al-polar to N-polar configurations. Thin films typically exhibit Al-polar characteristics at low doping concentrations (less than 1%), with no significant change in the piezoelectric coefficient d_{33}. However, as the doping concentration increases to 1-15 at%, a negative d_{33} value emerges, indicating a predominance of N-polar orientation. For Si concentrations above 15 at%, a gradual decline in d33 is observed. Undoped AlN typically consists of nanoparticles ranging from 15 to 35 nm in size and predominantly shows Al-polar characteristics. In contrast, the particle size of $Si_{0.11}Al_{0.89}N$ increases to 35-70 nm, corresponding with a stronger N-polar component. Anggraini *et al.*[15] further reported that with up to 15% Si doping, the c-lattice parameter decreases, while the a-lattice parameter slightly reduces, leading to a lower c/a ratio. This lattice contraction is attributed to the atomic size difference between Al (0.51 Å) and Si (0.42 Å). The size of the substituent atom is one factor influencing the ferroelectric response. Typically, an intermediate layer assists with polarity inversion in thin films. However, Anggraini's findings suggest that this mechanism may not be the dominant pathway for polarity reversal. X-ray photoelectron spectroscopy confirmed the presence of Si in the Si^{4+} state and Al in the Al^{3+} state. The substitution of Al^{3+} with Si^{4+} introduces point defects - specifically, Si_{Al} and aluminum vacancies (V_{Al}) - to maintain charge neutrality. As the Si concentration increases, the number of aluminum vacancies rises accordingly, and a correlation between these vacancies and polarity inversion has been established. This correlation is further corroborated by studies showing that Ge doping in AlN also induces polarity inversion from Al-polar to N-polar, likely due to the role of Ge in generating aluminum vacancies[95]. In that work, Mizuno *et al.*[95] observed a polarity switch accompanied by a shift in d_{33} from +7.8 to -7.7 pC/N. Notably, at a Ge

concentration of 2.8%, the d_{33} magnitude is comparable to that of undoped AlN. For Ge doping below 3%, the decrease in d_{33} can be attributed to a reduction in Al-polar domains as the Ge content increases [Figure 13]. Above this threshold, a gradual degradation in d_{33} is observed, potentially due to a decline in film crystallinity. A comparative analysis of the d_{33} responses in AlGeN and AlSiN reveals distinct trends based on doping concentration. A small amount of dopant promotes the transition from Al-polar to N-polar behavior, as indicated by a shift in d_{33} from positive to negative values.

For instance, the d_{33} values are approximately -1 and -5.4 pC/N for 0.8 at% Ge and 1 at% Si, respectively. The most pronounced negative d_{33} value, -6.3 pC/N for Si, corresponds to a transition from approximately +6.8 pC/N (N-polar polarization) observed at two different doping levels: 0.03 and 0.11. Si and Ge exhibit similar oxidation states (+1, +2, +3, +4), as well as comparable electronegativities and atomic radii, which likely accounts for their analogous effects in facilitating polarity inversion. This correlation reinforces the link between ferroelectric behavior and the choice of dopant element, as well as its influence on local atomic interactions. Notably, the asymmetry between the maximum negative and positive d_{33} values may be attributed to differences in electronegativity. The role of aluminum vacancies in polarity inversion can be interpreted through the formation of a defect complex, denoted as $[V_{Al} + nSi_{Al}]$, which may induce a transition in Si coordination from tetrahedral to octahedral geometry, resulting in the formation of IDBs. Additionally, codoping AlN with Mg and Si shows that when the Mg/Si ratio exceeds 1, d_{33} adopts a positive value, indicating a predominantly Al-polar thin film. Conversely, when the ratio is below 1, d_{33} becomes negative, corresponding to a primarily N-polar structure. The observed positive d_{33} value of 6 pC/N can be attributed to the oxidation states of Mg (+1, +2), which help compensate for the Al vacancies introduced by Si doping. At a Mg/Si ratio of 1, the d_{33} values are similar to those of undoped AlN films. The influence of codoping on local interactions is further evident from changes in particle size in Mg/Si codoped AlN films. For example, at a Mg/Si ratio of 0,4, particle sizes range from 40 to 80 nm, indicating a predominantly N-polar orientation. In contrast, a ratio greater than 1 results in a different morphology, with particle sizes ranging from 40 to 120 nm. Crystal structure analysis reveals a slight lattice contraction with increasing Si concentration, consistent with N-polar characteristics, while higher Mg concentrations lead to lattice expansion, reflecting Al-polar behavior. According to Anggraini and Takaaki Mizuno, elements with chemical characteristics similar to Si or Ge can induce ferroelectric behavior when doped into AlN, although variations in effect may arise due to differences in electronegativity and atomic radius. Zhu *et al.*[38] demonstrated a polarization wake-up process for ferroelectric switching in epitaxial $Al_{0.93}B_{0.07}N$ films grown on W-coated c-axis-oriented Al_2O_3 (sapphire) substrates. Doping AlN with 7 at% B stabilizes the as-deposited film in an N-polar state, as evidenced by rapid KOH etching of N-polar surfaces, which leaves behind residual grains and exposes the underlying tungsten substrate. Initial polarization cycling at 6 MV/cm shows negligible hysteresis, but with continued cycling, the hysteresis window gradually opens, and the remanent polarization exceeds 100 μC/cm². This wake-up behavior is governed by nucleation-dominated switching: the activation energy for domain nucleation during wake-up (0.15 ± 0.05 eV)[37] is significantly higher than that for polarization reversal in fully woken films (~0.028 eV)[38], confirming that early cycles primarily establish oppositely polarized nuclei rather than enabling large-scale domain wall motion. Frequency-dependent studies further demonstrate that the wake-up duration scales inversely with cycling frequency (~ 1 s at 50 Hz *vs.* ~ 0.5 s at 1,000 Hz), a phenomenon linked to transient self-heating (~ 11 K temperature rise) during high-frequency switching, which enhances defect mobility and accelerates domain wall propagation.

The crystalline asymmetry of the wurtzite structure, characterized by its polar surfaces (e.g., AlN(0001) and AlN(000-1)), plays a critical role in both polarization dynamics and thermal dissipation. Thermal analysis reveals that B-doped AlN maintains a high thermal conductivity (~ 12 W/m K), comparable to undoped

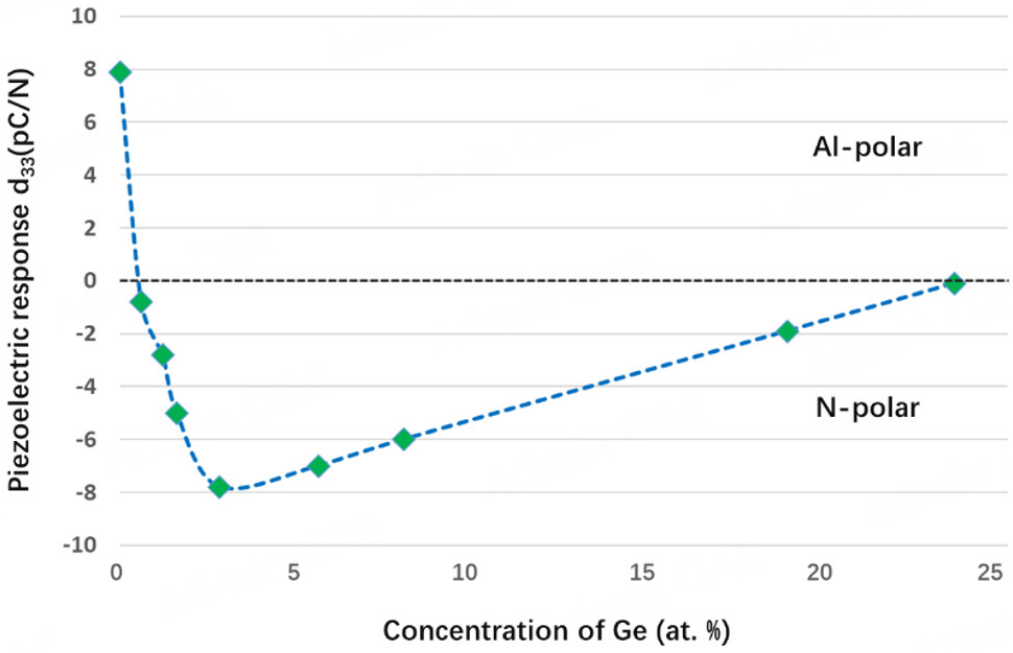

Figure 13. Dependence of the piezoelectric coefficient d_{33} on Ge concentration in $Ge_xAl_{1-x}N$ thin films. (Reproduced from Ref.[95]).

AlN and superior to Sc-doped AlN (< 9 W/m k[96]), where increased lattice distortion enhances phonon scattering. However, localized heating at polar interfaces during electrical cycling induces transient temperature spikes (~11 K), which accelerate nitrogen vacancy (V_N) migration toward domain walls and polar surfaces[37]. Over time, V_N aggregation at these interfaces degrades polarization retention and increases leakage currents, as confirmed by impedance spectroscopy, which shows a tenfold increase in conductivity in fatigued films. This leakage is further exacerbated by oxygen impurities (O_N) at the electrode interfaces, which artificially elevate the apparent polarization prior to dielectric breakdown. The choice of electrode material significantly affects endurance: Pt top electrodes withstand ~ 10^4 cycles, whereas tungsten electrodes extend device lifetimes to ~ 10^5 cycles due to lower resistivity and reduced Joule heating. Finite element simulations confirm that electric field crowding at electrode edges accelerates dielectric breakdown; however, this can be mitigated through field plate designs (e.g., SU-8 dielectrics with Pt guard rings), which homogenize the electric field distribution and extend endurance up to ~ 10^6 cycles. The interplay between polarization-induced field stress and thermal dissipation highlights the need for strategic substrate selection (e.g., sapphire for thermal stability) and interfacial engineering to suppress defect migration.

In boron-doped AlN, the polarization reversal process is ultimately nucleation-limited. As-deposited films crystallize in a polar phase with a uniform -P_r orientation and minimal domain wall density, which explains the initially low hysteresis. During early cycling, stable nuclei of oppositely polarized domains form once the applied electric field exceeds the critical threshold ($E > E_c$), while subsequent cycles promote domain wall motion and domain retraction. Complete volume switching requires achieving a critical density of nucleation sites, as domain wall propagation is spatially constrained during each cycle. This mechanistic framework underscores the importance of defect engineering and thermal management in optimizing wurtzite ferroelectrics for high-endurance applications such as non-volatile memory and piezoelectric sensors.

Tagantsev critiques the characterization of spontaneous polarization as a bulk property[97]. Posternak *et al.*[98] highlighted the challenges of evaluating spontaneous polarization in BeO under periodic boundary conditions. Martin further argued against deriving such polarization properties from unit cell calculations, citing intercellular charge transfer interactions and the influence of surface states[99]. In contrast, Resta *et al.*[100] supported an interpretation consistent with Landau's framework, suggesting that polarization can indeed be regarded as a bulk property. To reconcile these differing viewpoints - especially regarding the polarization current that arises during changes in system polarization - Resta proposed calculating polarization differences using the geometric or Berry phase, thus extending Landau's original definition[100]. Bernardini *et al.*[57,101] treated changes in polarization as a bulk quantity, evaluated using a periodic unit cell and assuming zero polarization for zinc blende as a symmetrical reference. Dreyer *et al.*[73] also explored an artificially constructed hexagonal phase with no polarization[72]. However, their results deviated substantially, with Dreyer reporting polarization values more than an order of magnitude higher than those obtained by Fiorentini *et al.*[57]. This inconsistency in spontaneous polarization calculations for wurtzite nitrides suggests potential limitations in the Berry phase methodology. Further complicating the issue, calculations by Yoo *et al.*[102] indicated non-zero polarization for zinc blende structures. Although wurtzite polarization is anticipated to be an intrinsic, reference-independent property, the striking discrepancies arising when using zinc blende or hexagonal phases as references suggest that the assumption of zero polarization in zinc blende warrants reexamination. If zinc blende possesses a polarization magnitude comparable to wurtzite, this could explain the inconsistencies observed. Strak *et al.*[103] argue that Spaldin's interpretation of polarization - focused primarily on surface charge contributions - can lead to misleading conclusions. Their analysis involved applying Spaldin's approach to wurtzite and zinc blende GaN slabs with well-defined surface terminations. Both structures exhibited non-zero polarization; however, due to the inherent symmetry of zinc blende GaN, it should theoretically exhibit zero polarization. Bulk polarization originates from electron displacement within covalent bonds, while surface contributions introduce edge effects. In covalent solids, this mechanism is primarily driven by charge transfer between the crystal lattice and atomic orbitals. For both wurtzite and zinc blende lattices, it is crucial to consider the role of bonding tetrahedra in the emergence of polarization. Spaldin's emphasis on surface charges conflates bulk and surface effects, potentially leading to incorrect interpretations of polarization behavior. Surface effects must be properly accounted for and subtracted. To address these issues and improve the accuracy of spontaneous polarization calculations in materials such as wurtzite and zinc blende, Strak *et al.*[103] proposed a refined methodology based on four key principles: (1) Defining polarization as a bulk property: Polarization is treated as an intrinsic property of the bulk material, independent of surface effects; (2) Separating bulk and surface contributions: Bulk polarization is isolated using a single-cell model with periodic boundary conditions; (3) Considering atomic contributions: Polarization is calculated as the sum of dipole moments from individual atoms, based on the surrounding electron charge distribution; and (4) Avoiding symmetry breaking: The geometry of the computational cell is designed to preserve the crystal's inherent symmetry, preventing artificial polarization contributions. This revised approach aims to clarify and enhance the accuracy of polarization calculations in these structurally complex materials.

Doping AlN with Sc has been shown to induce ferroelectric behavior, with both the response and quality of the hysteresis loop being dependent on the Sc content. Therefore, a comparative analysis of Sc doping effects in AlN *vs.* other related films is critical. Uehara *et al.*[104] demonstrated ferroelectric behavior in $Ga_{1-x}Sc_xN$[104], showing a remanent polarization exceeding 120 μC/cm² - comparable to that of $Al_{1-x}Sc_xN$ - but with a lower coercive field at similar remanent polarization levels. Additionally, variations in the c/a ratio and average u-parameter with increasing Sc concentration showed similar trends in both $Ga_{1-x}Sc_xN$ and $Al_{1-x}Sc_xN$: c/a decreased while u increased. Hysteresis was observed in the P-E measurements for x = 0.41 and 0.44 at 300 K, but was absent at x = 0.35. However, heating the film to 423 K led to a gradual opening of the hysteresis window, revealing remanent polarization and producing results comparable to those of

$Al_{1-x}B_xN$. This hysteresis behavior is influenced by both Sc concentration and temperature, which correlates with increased domain wall density. Although domain wall mobility remains low, the higher density facilitates polarization switching. These findings suggest a critical limit on the dopant ratio required to achieve a ferroelectric response. This limit is governed by several factors, including oxidation state, electronegativity, and atomic radius. The presence of dopants is essential for forming Inverted Domain Boundaries, which may enhance ferroelectric switching through changes in these parameters. Analysis using positive-up negative-down measurements indicates that saturation of remanent polarization is contingent on Sc concentration, temperature, and the applied electric field.

For Sc concentrations of 0.41 and 0.44, remanent polarization saturation remained consistent across all measurement temperatures but varied with electric field strength. Notably, for x = 0.41 at 473 k and x = 0.44 at both 423 and 473 k, a similar electric field (≈ 3 MV/cm) was required to achieve saturation. This suggests a maximum density of compatible domain walls for polarization switching. These observations align with previous findings of structural degradation in the wurtzite phase, reduced ferroelectric response, and phase transitions to cubic structures. Comparisons of remanent polarization and coercive field among $Ga_{1-x}Sc_xN$, $Al_{1-x}Sc_xN$, and $Al_{1-x}B_xN$ show that remanent polarization saturation is largely temperature-dependent, suggesting it is an intrinsic structural property. Meanwhile, the coercive field decreases with increasing temperature, highlighting the low mobility of domain walls. Furthermore, at equivalent Sc concentrations, $Ga_{1-x}Sc_xN$ exhibits higher remanent polarization than $Al_{1-x}Sc_xN$, attributed to the greater electronegativity difference between Ga (1.81) and Sc (1.36) compared to Al (1.61) and Sc. This difference produces more polarized electron distributions in Ga-Sc bonds than in Al-Sc bonds, leading to larger partial charges and higher remanent polarization. While factors such as ion substitution, crystal structure, and defects also influence remanent polarization, electronegativity differences play a particularly significant role. It has also been observed that the coercive electric field (Ec) of wurtzite materials is more strongly affected by Sc concentration than by the u-parameter. Although the u-parameter can reflect polarization levels, it is less sensitive to polarization switching resistance. In a recent study, Lee *et al.*[105] refuted the earlier design principle that linked lower c/a lattice ratios to lower switching barriers (i.e., Ec values)[105]. Instead, they identified two more reliable design principles: ionicity and bond strength - the latter being unaffected by the u-parameter. Among these, ionicity appears to be a more favorable parameter for engineering future ferroelectric materials, particularly through alloying. Higher ionicity generally correlates with larger electronic band gaps, while materials with lower bond strength (softer materials) tend to have narrower band gaps. The study also found that over 90% of candidate wurtzite-type materials suitable for military applications prefer alternative switching pathways involving novel non-polar, metastable structures. These findings highlight the need for a deeper understanding of switching mechanisms and the importance of ionicity and bond strength in designing next-generation low-power ferroelectric devices.

In the context of polarization switching, several key factors govern the effects of metal doping in AlN and related wurtzite structures:

• Type of metal dopant: Different dopants have markedly different effects on ferroelectric properties. For example, Sc-doped AlN shows enhanced remanent polarization and reduced coercive fields compared to AlN doped with Mg or Zn.

• Dopant concentration: Increasing dopant concentration typically enhances remanent polarization and reduces coercive fields; however, excessive doping can negatively impact ferroelectric behavior.

• Crystal structure: The underlying crystal structure is critical. Sc doping maintains the wurtzite structure favorable for ferroelectricity, while Mg doping tends to result in a zinc blende structure, which is less conducive.

Additional nuances include:

• The effects of metal doping on polarization switching vary among different wurtzite structures.

• Dopant concentration continues to play a key role in determining ferroelectric properties.

• Material defects introduced by doping also influence ferroelectric behavior.

Notably, doping AIN with metals such as Mg, Zn, and Y has shown positive effects on polarization switching. Generally, dopants with a larger ionic radius than Al reduce the coercive field. Conversely, Ga doping tends to increase E_c due to the additional positive charge, which hinders polarization switching. Table 2 summarizes the relationship between atomic radius and electronegativity of the dopant and substituted atoms. A lower electronegativity generally correlates with a larger ionic radius, while a higher electronegativity results in a smaller radius. Understanding this correlation may aid in optimizing ferroelectric performance in wurtzite structures.

The study by Momida *et al.*[40] further supports this trend, demonstrating notable enhancements in the piezoelectric constants of ABN through the substitution of Al, Ga, and In with Sc, Y, and La - elements characterized by larger atomic radii and lower electronegativity[40].

Exploring the relationship between electronegativity and atomic radius offers promising directions for engineering dopants to improve the polarization-switching characteristics of wurtzite structures. In particular, dopants with lower electronegativity and larger atomic radii have been shown to effectively reduce the coercive field. Ongoing research underscores the importance of this correlation in precisely tuning the ferroelectric properties of wurtzite materials.

Although factors such as material defects and temperature also influence the ferroelectric behavior of doped AlN and related wurtzite structures, the type and concentration of the metal dopant, along with the intrinsic crystal structure, are the most critical determinants. Table 3 summarizes the effects of various metal dopants on the ferroelectric properties of AIN. Notably, Sc-doped AlN exhibits the highest remanent polarization and the lowest coercive field, whereas Zn-doped AlN shows the opposite trend, with the lowest remanent polarization and the highest coercive field.

ALD OF DOPED ALN: A PROMISING FUTURE

$Al_{1-x}Sc_xN$ alloys have emerged as key materials for advanced ferroelectric and piezoelectric applications due to their exceptional electric breakdown strength (ranging from 2 to 5 MV/cm), which enables the use of thinner ferroelectric layers in memory devices without compromising the memory window. However, integrating these materials into low-voltage systems remains challenging, despite their improved polarization stability and retention at elevated temperatures. Key hurdles include achieving phase purity, minimizing oxygen contamination (due to the high oxygen affinity of Al and Sc, which necessitates a high-vacuum environment during AlScN growth), and maintaining high crystal quality while ensuring industrial scalability. Although deposition techniques such as sputtering, MOCVD, MBE, and PLD have contributed

Table 2. Relationship between the atomic radius and electronegativity of dopant and substituted elements

Element	Electronegativity	Atomic radius (pm)	Covalent radius (pm)	Van der Waals radius (pm)
Al	1.61	143	121 ± 4	184
Sc	1.36	162	170 ± 7	211
Zn	1.65	134	122 ± 4	139
Mg	1.31	160	141 ± 7	173
Ga	1.81	135	122 ± 3	187
Sc	1.36	162	170 ± 7	211
Al	1.61	143	121 ± 4	184
B	2.04	90	84 ± 3	192

Table 3. Effects of different metal dopants on the ferroelectric properties of AlN

Metal dopant	Remanent polarization ($\mu C/cm^2$)	Coercive field (MV/cm)
Sc	110	1.5
Mg	85	4.5
Zn	60	9

to the advancement of AlScN growth, each method has inherent limitations in terms of defect density, film uniformity, or scalability. In this context, Atomic Layer Deposition (ALD) offers a transformative approach, providing atomic-level precision, CMOS compatibility, and conformal coating capabilities - features that are critical for next-generation devices.

Sputtering: scalability *vs.* microstructural defects

Sputter deposition is a widely used method for producing $Al_{1-x}Sc_xN$ films with strong c-axis orientation, employing either Al/Sc alloy targets or dual-metal co-sputtering. While alloy targets improve deposition rates and composition uniformity, co-sputtering allows for tunable Sc concentration, albeit often at the expense of film homogeneity. In a pioneering study, Akiyama *et al.*[60] demonstrated the epitaxial growth of AlScN via reactive RF dual magnetron sputtering on Si (001) substrates. Subsequent research has confirmed the successful growth of c-axis-oriented (0001) AlScN films using reactive magnetron co-sputtering on both silicon and sapphire substrates. However, sputtered films often contain trace amounts of oxygen and suffer from difficulties in achieving a uniform in-plane orientation. This typically results in columnar growth with high threading dislocation densities at grain boundaries, complicating efforts to obtain high crystal quality. These challenges increase the likelihood of defects such as abnormally oriented grains, stemming from the alloy's multiple phases. Controlling the Sc content via alloy targets involves complex metallurgical processes, which can drive up production costs. Co-sputtering offers a more economical alternative, allowing Sc concentration to be tuned by adjusting the power of individual targets. However, this approach may compromise film uniformity and crystallinity. To meet the demands of low-power memory applications and ensure CMOS compatibility, the deposited films must support low-voltage operation and enable low-temperature growth on Si substrates.

Despite these challenges, Liu *et al.*[48] reaffirmed the feasibility of sputtering for BEOL-compatible AlScN[48]. Their process, conducted in a PVD system without vacuum interruption, achieved excellent reproducibility, with thickness variation within ±1 nm, at CMOS-compatible temperatures (< 350 °C). Furthermore, the use of KOH wet etching for patterning Al electrodes aligns well with standard industrial workflows. These findings highlight sputtering's continued relevance for scalable, low-cost production of ultra-thin ferroelectric films, complementing ALD's advantages in conformal coating.

MOCVD: high growth rates *vs.* precursor limitations

MOCVD has become the method of choice for the large-area, uniform growth of nitride semiconductors, primarily due to its high growth rates (up to several microns per hour) compared to MBE. However, a key challenge facing MOCVD is the limited availability of effective scandium precursors with sufficiently high vapor pressure - a limitation rooted in scandium's classification as a group III-B transition metal. Historically, the low vapor pressure of available precursors has restricted Sc incorporation to doping-level concentrations only[61,106]. Recent developments have introduced scandium precursors with high vapor pressures, representing a significant advancement in this domain. Notably, the Cp_3Sc precursor has been utilized in studies that systematically vary parameters such as growth temperature, growth mode, III/V ratio, and reactor pressure to optimize growth conditions[107-109]. Despite these improvements, growth rates using Cp_3Sc remain low (~0.006 nm/s), resulting in prolonged thermal exposure and increased interfacial diffusion.

Molecular beam epitaxy (MBE) enables the growth of single-crystalline $Al_{1-x}Sc_xN$ under ultra-high vacuum (approximately 10^{-10} torr). Early research relied on sputter deposition methods, which typically produced polycrystalline films with textured surfaces[110]. However, recent advancements in MBE have enabled the fabrication of ferroelectric AlScN and GaScN thin films with single-crystalline quality[91,111-114]. These high-quality films have facilitated device miniaturization down to ~5 nm and supported the development of various ferroelectric devices, including ScAlN/GaN heterostructure memories, ScAlN/GaN HEMTs, and ScAlN-based self-powered photodetectors[111,115]. The MBE process involves directing atomic or molecular beams from solid sources of group III elements (Al, Ga, In, Sc) onto a heated substrate. Crucible temperature controls the vapor pressure of each element. In this molecular regime, the evaporated atoms experience minimal collisions before reaching the substrate. A significant breakthrough was reported in 2017 when researchers successfully grew single-crystal AlScN on GaN using radio-frequency plasma-assisted MBE. Their findings showed that metal-rich growth conditions influence phase purity by promoting the formation of intermetallic compounds. Nitrogen is introduced via radical-generating sources or through thermal cracking of ammonia (NH_3) on the substrate. Sufficient nitrogen flow is critical for achieving smooth III-nitride films. MBE growth of AlScN typically requires substrate temperatures above 500 °C. In addition to GaN, AlScN epitaxy can be achieved on substrates such as AlN, SiC, Al_2O_3, and Mo via MBE, MOCVD, or PLD. MBE offers the advantage of producing ultra-thin epitaxial films with high uniformity and the ability to engineer multilayer structures with precisely controlled doping or compositional variations[116]. Nevertheless, MBE suffers from low throughput (~0.1-1 nm/s) and high equipment costs, limiting its viability for industrial-scale applications and confining its use largely to research settings.

By maintaining a substrate temperature of 700 °C and precisely controlling the Sc/Al flux ratio, Wang *et al.*[72] achieved lattice-matched AlScN films on GaN/sapphire templates, eliminating strain-induced dislocations. The lattice-matched interface minimized dislocation-mediated leakage, thereby improving electron mobility by reducing alloy disorder scattering. However, their study also revealed that Sc's high affinity for oxygen leads to rapid surface oxidation upon air exposure, forming Sc-O and Al-O bonds. This oxidation disrupts polarization switching and complicates band alignment measurements - both critical to heterostructure device design. These findings underscore MBE's strength in achieving structural perfection. Mitigation strategies such as ultra-high-vacuum storage and atomic layer deposition of encapsulation layers are essential to preserve the ferroelectric and piezoelectric properties of AlScN in practical devices.

PLD: stoichiometric control *vs.* throughput limitations

PLD offers distinct advantages, particularly its precise stoichiometric transfer from target to substrate, which is essential for stabilizing the metastable wurtzite phase - especially at high Sc concentrations. Recent

studies[117] have demonstrated the successful growth of high-quality, single-crystalline ferroelectric $Al_{1-x}Sc_xN$ films using PLD, achieving Sc concentrations up to x = 0.3 while maintaining minimal oxygen contamination (≤ 0.1 at%) and excellent structural integrity. Advanced characterization techniques, including XRD and aberration-corrected STEM, confirmed a domain-matching epitaxial relationship with sapphire substrates, resulting in sharp interfaces and reduced lattice mismatch. These PLD-grown films exhibit impressive properties: a spontaneous polarization of 140 μC/cm², a fivefold increase in the piezoelectric coefficient (d_{33} ≈ 10 pm/V) compared to undoped AlN, and ultralow leakage currents (5×10^{-5} A/cm² at 4 MV/cm). These features address common issues such as high leakage and inhomogeneity typically observed in polycrystalline sputtered films. Moreover, the films demonstrate thermal stability up to 600 °C and compatibility with CMOS processes, underscoring their promise for high-frequency RF filters, non-volatile memories, and high-temperature electromechanical devices. Building on these achievements, high-throughput PLD (HT-PLD) has emerged as a potentially transformative technique for accelerating the development of $Al_{1-x}Sc_xN$ materials. Inspired by breakthroughs in complex oxides such as $SrTiO_3$ (STO), where HT-PLD enabled efficient screening of thickness-dependent properties[118], this approach offers significant benefits for tackling key challenges in AlScN - such as doping optimization, phase stability, and the role of defects (e.g., oxygen vacancies) that influence leakage and polarization behavior. HT-PLD enables rapid exploration of vast processing parameter spaces, aligning with materials genome initiatives and helping elucidate how factors like thickness and defect distributions affect interfacial barriers and domain switching - critical for low-power memory and RF applications. The scalability and precision of HT-PLD may also enable uniform fabrication required for integrating AlScN into neuromorphic computing systems or multifunctional devices that leverage its dual piezoelectric-ferroelectric functionality, such as ultra-low-loss acoustic resonators or advanced haptic interfaces.

Despite these advantages, conventional PLD faces limitations that hinder industrial scalability, including low deposition rates (~ 0.1 nm/s) and difficulties in achieving uniform coverage over large areas. To overcome these barriers, future research must prioritize three key areas: (1) defect control using *in-situ* metrology and machine learning-driven process optimization; (2) enhancement of phase stability through predictive doping strategies; and (3) functional device demonstrations (e.g., ferroelectric FinFETs, ultra-wideband RF filters) to validate performance in real-world environments. Addressing these challenges could enable PLD-grown AlScN to realize its full potential in applications such as neuromorphic computing, 6G communications, and high-temperature MEMS, firmly establishing its role in next-generation semiconductor technologies.

AlScN microstructure: strongly dependent on deposition conditions

Yang *et al.*[119] investigated the effect of substrate temperature on the microstructural characteristics of $Sc_{0.1}Al_{0.9}N$ films deposited on Si(100) substrates. By varying the deposition temperature from room temperature to 650 °C, they observed a pronounced influence on the film's microstructure. Optimal crystallinity was achieved at a substrate temperature of 600 °C, yielding a rocking curve full width at half maximum (FWHM) of 4°. At this temperature, the root mean square (RMS) surface roughness was also minimized, reaching 2.4 nm. Zukauskaite *et al.*[120] presented θ-2θ X-ray diffraction patterns for $Al_{1-x}Sc_xN$ films with scandium contents of 0%, 20%, and 30%, deposited at 400, 600, and 800 °C. Their analysis revealed that increasing scandium content and deposition temperature led to a degradation in microstructural quality, as evidenced by decreased diffraction peak intensity. Interestingly, this behavior contrasts with that of pure AlN, which remains relatively stable between 400 and 600 °C, showing only slight degradation at 800 °C. Pérez-Campos *et al.*[121] studied $Al_{0.6}Sc_{0.4}N$ films deposited on Si(100) substrates, varying gas pressure (0.26-1.06 Pa) and DC power (300-900 W). They found that the highest power setting of 900 W produced the narrowest rocking curve, indicating superior crystallinity. However, the differences in microstructure among films deposited at 500, 700, and 900 W are marginal. In contrast, films deposited

at 300 W, especially at pressures above 0.6 Pa, exhibited significantly poorer microstructural quality.

Overall, these studies underscore that the microstructure of $Al_{1-x}Sc_xN$ films is highly sensitive to deposition parameters, suggesting that their intrinsic properties are tightly linked to the quality of their crystalline structure.

ALD: bridging precision and scalability

The rise of organic flexible substrate electronics has driven the need for low-temperature processing techniques. Concurrently, ongoing trends in device miniaturization and the demand for precise control over film thickness, deposition parameters, and defect density have positioned ALD as a key enabling technology for next-generation semiconductor devices. Van der Wel *et al.*[122] introduced an innovative approach to area-selective ALD of AlN films. This technique enables AlN to be deposited exclusively on designated regions of a patterned substrate, which is critical for electronic applications requiring selective material placement. The process begins with substrate pretreatment to remove native AlO_xN_y, facilitating targeted AlN growth. A key factor in this method is the use of distinct surface terminations: sputtered AlN for the growth surface and thermal SiO_2 for the non-growth surface. The authors propose that methylation of the non-growth surface with trimethylaluminum (TMA) effectively inhibits AlN deposition in those areas. This strategy may also be applicable to other nitride materials, such as GaN. Their findings represent a promising strategy for the high-precision deposition of AlN thin films.

III-Nitrides, especially AlN, show great promise for use in high-power electronics, optoelectronic devices, sensors, and transistors. However, several challenges remain, including difficulty in nitrogen incorporation, a lack of suitable native substrates, reliance on thick buffer layers, and high deposition temperatures that hinder compatibility with chip fabrication - particularly during Back-End-Of-Line processes. ALD has emerged as a viable alternative for next-generation III-Nitride applications, enabling the growth of sub-10 nm films through surface-controlled precursor reactions. This method allows for conformal coating of complex geometries with exceptional thickness control and uniformity across large areas. ALD-based AlN deposition has been explored for over three decades, typically using TMA as the metal precursor and ammonia (NH_3) as the nitrogen precursor, alongside various combinations of nitrogen and aluminum precursors[90,123-127]. Despite efforts to optimize precursor combinations, many reactions still suffer from inefficient stoichiometry, with low nitrogen-to-metal precursor ratios. The high consumption of precursor gases and the accumulation of unreacted nitrogen necessitate additional treatment equipment, increasing system complexity and cost, thus limiting mass-production viability. A key limitation stems from the use of metal-carbon bonded precursors, which complicate ammonia dissociation. To address this, researchers are exploring alternative precursors that directly bond metal and nitrogen atoms, potentially easing ammonia activation. Promising candidates include formamidinates, amidinates, trisguanidinates, and triazenides[128-130]. Seppänen *et al.*[131] proposed an Atomic Layer Annealing method, applying a 20-second Ar plasma pulse at 200 W after each deposition cycle to improve stoichiometry, crystallinity, and *c*-axis orientation while reducing carbon and hydrogen impurities. Similarly, Shih *et al.*[132] achieved high-quality AlN thin films using Plasma-Enhanced ALD (PE-ALD) coupled with *in situ* Atomic Layer Annealing, transforming amorphous AlN into a single-crystalline epitaxial film at a relatively low deposition temperature of 300 °C. Kao *et al.*[133] further demonstrated that electron beam annealing can enhance the density of epitaxial AlN layers while minimizing damage, making it suitable for low-temperature deposition. Despite the growing body of research on ALD-deposited AIN, studies on doped AlN remain limited, with fewer than 20 publications in the ALD database addressing doped AlN[134]. Nepal *et al.*[135], in work on $Al_xGa_{1-x}N$ and $In_xAl_{1-x}N$, demonstrated that ALD can achieve wide stoichiometric ranges, even in cases where phase separation occurs using other deposition methods - highlighting ALD's potential to overcome miscibility gaps and challenges associated with conventional growth techniques.

Tian *et al.*[136] explored the use of hydrogen plasma to enhance the reactivity between TMA and NH_3 precursors. Their study reported very low oxygen and carbon contamination (around 1.5% and 1%, respectively) and fewer C-Al bonds in PE-ALD samples compared to those produced by thermal ALD. This suggests that H_2 plasma may aid in breaking Al-CH_3 bonds in TMA or increasing the NH_3 reactivity. Notably, lower H_2 flow rates resulted in polycrystalline films with poor crystallinity, while higher H_2 flow rates yielded films with a (002) preferred orientation, contrasting with the (0010) orientation commonly seen in thermal ALD. Ozgit *et al.*[137] achieved a constant growth rate of 0.86 Å/cycle over the 100 to 200 °C range, even at very low deposition temperatures. Additionally, variations in plasma generation methods - such as direct inductively coupled plasma and indirect capacitively coupled plasma - have been shown to affect AlN growth[138], influencing growth per cycle (e.g., up to 1.54 Å/cycle), total cycle duration, homogeneity, and residual oxygen content. Thus, plasma type and configuration should be carefully considered during process optimization. Optimizing growth conditions - such as substrate temperature, growth pressure, and gas flow rates - is crucial for achieving desired film microstructures, enhancing crystallinity, and minimizing defect densities. Techniques such as high-purity precursors, *in situ* cleaning, and carefully tuned deposition parameters can contribute significantly to the quality of doped AlN films. The choice between PLD and ALD for doped AlN synthesis hinges on specific application requirements. PLD is ideal for producing high-quality epitaxial films with precise stoichiometry, low oxygen contamination, and excellent thermal stability, making it suitable for high-performance, research-grade devices. ALD, in contrast, excels in providing conformal coatings on complex 3D structures with sub-nanometer thickness control - critical for CMOS compatibility and industrial scalability. However, ALD faces challenges in incorporating refractory dopants like Sc due to precursor limitations and often requires post-deposition annealing, which can degrade film or interface quality. While sputtering, MBE, and PLD have advanced AlScN research, ALD's unparalleled precision, conformality, and scalability address key challenges in doping control, defect engineering, and process integration. Recent advances in precursor chemistry, plasma engineering, hybrid deposition techniques, and post-processing have begun to address these limitations. As semiconductor technologies continue to scale down and require ultrathin, low-power ferroelectrics, ALD is increasingly seen as a cornerstone of future nitride semiconductor development.

The convergence of ALD's conformality with PLD's epitaxial precision may enable the creation of defect-engineered heterostructures for applications such as RF filters and neuromorphic computing. Ultrathin ALD-grown AlScN (< 10 nm) with low leakage current supports low-voltage memory applications, while low-temperature deposition on flexible substrates opens the door to wearable sensors. Scalable methods such as multi-target PLD and HT-PLD, combined with ALD's atomic-level control, position doped AlN at the forefront of high-frequency resonators, self-powered photodetectors, and haptic interface technologies.

Table 4 summarizes the advantages and disadvantages of various thin-film growth methods, including Magnetron Sputtering, MBE, ALD, and PLD.

CONCLUSIONS

Metal doping has emerged as a promising strategy to enhance the polarization-switching characteristics of wurtzite AlN thin films. The selection and concentration of dopants can vary among different wurtzite structures and are influenced by inherent material defects. These factors affect film polarity, polarization magnitude, and switching behavior. The proposed polarization-switching mechanisms in wurtzite AlN are closely linked to the dopant species, which significantly influence polarization dynamics. Furthermore, intrinsic material defects can serve as nucleation sites for domain walls, playing a key role in the switching process. Investigations into AlScN and other doped wurtzite materials have revealed complex interactions among structural, chemical, and electronic factors that govern their ferroelectric properties. Critical to this

Table 4. Advantages and disadvantages of common thin-film deposition methods

Feature	Magnetron sputtering	Molecular beam epitaxy (MBE)	Atomic layer deposition (ALD)	Pulsed laser deposition (PLD)
Typical growth temp.	Low to moderate (< 400 °C possible)	Moderate to high (Often > 600 °C)	Low to moderate (Often 200-400 °C)	Moderate to high (Substrate heating required)
Film quality	Good Polycrystalline (textured films possible)	Excellent epitaxial/single-crystal	Variable (from amorphous to polycrystalline)	Good epitaxial/polycrystalline films possible
Purity	Good (depends on target purity)	Very high (UHV environment)	Variable (depends on precursor purity/residues)	Good (Stoichiometric transfer possible)
Uniformity	Good (suitable for large-area deposition)	Moderate (requires substrate rotation for uniformity)	Excellent	Moderate (Can be challenging over large areas)
Scalability/throughput	High	Low	Moderate (Batch processing possible)	Moderate (Combinatorial approaches possible)
Conformality	Low to moderate	Low	Excellent	Low to moderate
CMOS compatibility	High (Low temp., BEOL integration possible)	Moderate (higher temp.)	High (Low temp., BEOL integration possible)	Moderate (temp. and particulates are concerns)
Key advantages	Scalable, CMOS-compatible, widely adopted	Highest quality/purity, Precise control	Conformality, thickness control	Versatile, enables Stoichiometric material transfer
Key disadvantages	Limited conformality, potential defects	Slow, expensive, high temp. required	Slow, precursor-related challenges, variable purity	Particle generation, Uniformity issues

behavior is the local atomic environment, particularly the coordination of Sc and Al atoms, which strongly influences the polarization-switching mechanism. The nature of the chemical bonding, shaped by the dopant's electronegativity and atomic radius, critically impacts the energy barrier for polarization reversal. Various deposition techniques - such as atomic layer deposition (ALD), molecular beam epitaxy (MBE), and sputtering - offer distinct advantages and limitations in fabricating high-quality AlScN films with tailored properties. ALD, in particular, provides precise control over film thickness and composition, though it may face challenges related to precursor chemistry and slower growth rates. Future investigations should prioritize elucidating the fundamental switching mechanisms, optimizing doping strategies, improving film quality, and developing innovative device architectures. Studies on B-doped AlN suggest promising directions for optimizing wurtzite ferroelectrics. Hybrid doping strategies (e.g., $Al_{1-x-y}B_xSc_yN$) may combine the low coercive field of Sc with the high thermal stability of B, although miscibility issues remain a challenge. Moreover, device designs such as field plates and ALD-grown encapsulation layers (e.g., Al_2O_3) could mitigate oxidation and defect migration, potentially extending the operational lifetime of non-volatile memory devices. Future work should explore transient thermal modeling to address self-heating in high-frequency RF devices and investigate combinatorial doping approaches (e.g., B + Y, B + La) to decouple polarization switching from lattice strain. Addressing these challenges, while leveraging the unique properties of AlScN and related doped wurtzite materials, may enable the development of next-generation devices with outstanding performance and reliability. Although the study of metal doping effects on polarization switching in wurtzite AlN is still in its early stages, careful selection of dopant types and concentrations can yield films with optimized polarity, polarization strength, and switching characteristics. Doping with rare-earth elements presents stability challenges, for which ALD may offer a robust solution. Given the high costs of rare-earth elements, researchers such as Startt *et al.*[18] have recommended using group IVB metals as a more economical alternative.

Table 5 summarizes various $Al_{1-x}Sc_xN$-based layers with different Sc concentrations fabricated using a range of deposition methods.

Table 5. Summary of $Al_{1-x}Sc_xN$-based layers with different Sc concentrations fabricated using various deposition methods

No.	Unit	Author	Style of deposition	Al-Sc-based system	Thickness	Ratio	E_c	Pr	References
1	University of Kiel/Germany	Georg Schönweger Simon Fichtner	Sputtering	$Al_{1-x}Sc_xN$	5 nm	x = 0.26	2.1 MV/cm	-	[6]
2	Albert-Ludwigs University/Germany	Jana Lig Stefano Leone	MOCVD	$Al_{0.7-x}NixSc_{0.3}N$	10 nm	x = 0.14	-	-	[139]
3	University of Freiburg/Germany	Kathrin Frei	MBE	$Al_{1-x}Sc_xN$	20 nm	x = 0.02-0.69	-	-	[140]
4	University of Pennsylvania/USA	Dixiong Wang Roy H. Olsson	Sputtering	$Al_{1-x}Sc_xN$	20 nm	x = 0.32	6.5 MV/cm	140 μC/cm^2	[141]
5	Tokyo Institute of Technology/Japan	Junji Kataoka	Sputtering	$Al_{1-x}Sc_xN$	30 nm	x = 0.22	-	-	[142]
6	Tokyo Institute of Technology/Japan	Si-Meng Chen	Sputtering	$Al_{1-x}Sc_xN$	30-40 nm	x = 0.26	-	-	[143]
7	Seoul National University/Republic of Korea	Seung Kyu Ryoo Cheol Seong Hwang	Sputtering	$Al_{1-x}Sc_xN$	20 nm 45 nm	x = 0.3	6.5 MV/cm (20 nm) 6.0 MV/cm (45 nm)	60 μC/cm^2 (20 nm) 110 μC/cm^2 (45 nm)	[144]
8	University of Pennsylvania/USA	Xiwen Liu Roy H. Olsson Deep Jariwala	Sputtering	$Al_{1-x}Sc_xN$	100 nm	x ≥ 0.27 x = 0.29	2-4.5 MV/cm /	80-115 μC/cm^2 80 μC/cm^2	[8]
9	University of Michigan/USA	Ping Wang Ding Wang Zetian Mi	MBE	$Al_{1-x}Sc_xN$	100 nm	x = 0.2	4.2 MV/cm	135 μC/cm^2	[145]
10	University of North Western Industry/China	Bingcheng Luo	Sputtering	$Al_{0.7-y}Ni_ySc_{0.3}N$	189 nm	x = 0.3	3 MV/cm	100 μC/cm^2	[146]
11	Naval Research Laboratory/USA	Matthew T. Hardy	MBE	$Al_{1-x}Sc_xN$	200 nm	x = 0.16-0.18	-	-	[147]
12	Naval Research Laboratory/USA	Matthew T. Hardy	MBE	$Al_{1-x}Sc_xN$	200 nm	x = 0.06-0.32	-	-	[148]
13	University of Kiel/Germany	Simon Fichtner	Sputtering	$Al_{1-x}Sc_xN$	400 nm 600 nm 1,000 nm	x = 0.27 x =0.32/0.36/0.40 x = 0.43	5 MV/cm at x = 0.27 max	110 μC/cm^2 at x = 0.27 max	[46]
14	University of Craiova/Romania	Cosmin Silviu Sandu	Sputtering	$Al_{1-x}Sc_xN$	500 nm	x = 0.00-0.43	-	-	[149]
15	Georgia Institute of Technology/USA	Jialin Wang	Sputtering	$Al_{1-x}Sc_xN$	900 nm	x = 0.3	0.2 MV/cm	80 μC/cm^2	[150]
16	Fraunhofer Institute for Silicon Technology (ISIT) & University of Kiel/Germany	Tom-Niklas Kreutzer Simon Fichtner	Sputtering	$Al_{1-x}Sc_xN$	500 + 500 nm	x = 0.35	-	-	[151]

DECLARATIONS

Authors' contributions

Conceptualization, validation, formal analysis, resources, writing - original draft preparation: Saadi, M.
Visualization: Shao, W.
Project administration: Tong, Y.
Methodology, data curation: Saadi, M.; Shao, W.
Funding acquisition: Wang, X.; Tong, Y.
Writing - review and editing: Saadi, M.; Wang, X.; Tong, Y.
Investigation: Saadi, M.; Han, C.; Zhang, M.; Shao, W.
Supervision: Wang, X.; Zhang, H.; Tong, Y.; Hu, Y.
Methodology, investigation: Qin, H.
All authors have read and agreed to the published version of the manuscript.

Availability of data and materials

Not applicable.

Financial support and sponsorship

This work was funded by the 2030 Major Project of the Chinese Ministry of Science and Technology, grant No. 2021ZD0201200, and the High-End Foreign Expert Team of the Ministry of Science and Technology, grant No. G2022178034L. This work was also supported in part by the research fund of the Suzhou laboratory (No. SK-1202-2024-012).

Conflicts of interest

All authors declared that there are no conflicts of interest.

Ethical approval and consent to participate

Not applicable.

Consent for publication

Not applicable.

REFERENCES

1. Yasuoka, S.; Shimizu, T.; Tateyama, A.; et al. Effects of deposition conditions on the ferroelectric properties of $(Al_{1-x}Sc_x)N$ thin films. *J. Appl. Phys.* **2020**, *128*, 114103. DOI
2. Lin, B. T.; Lee, W. H.; Shieh, J.; Chen, M. J. Ferroelectric AlN ultrathin films prepared by atomic layer epitaxy, In Proceedings Behavior and Mechanics of Multifunctional Materials XIII; 2019. DOI
3. Hasegawa, K.; Shimizu, T.; Ohsawa, T.; Sakaguchi, I.; Ohashi, N. Full polarization reversal at room temperature in unsubstituted AlN. *Appl. Phys. Lett.* **2023**, *123*, 192903. DOI
4. Skidmore, C. H.; Spurling, R. J.; Hayden, J.; et al. Proximity ferroelectricity in wurtzite heterostructures. *Nature* **2025**, *637*, 574-9. DOI
5. Kim, K. H.; Han, Z.; Zhang, Y.; et al. Multistate, ultrathin, back-end-of-line-compatible AlScN ferroelectric diodes. *ACS. Nano.* **2024**, *18*, 15925-34. DOI
6. Schönweger, G.; Wolff, N.; Islam, M. R.; et al. In-grain ferroelectric switching in sub-5 nm Thin $Al_{0.74}Sc_{0.26}N$ films at 1 V. *Adv. Sci.* **2023**, *10*, e2302296. DOI PubMed PMC
7. Zheng, J. X.; Fiagbenu, M. M. A.; Esteves, G.; et al. Ferroelectric behavior of sputter deposited $Al_{0.72}Sc_{0.28}N$ approaching 5 nm thickness. *Appl. Phys. Lett.* **2023**, *122*, 222901. DOI
8. Liu, X.; Wang, D.; Kim, K. H.; et al. Post-CMOS compatible aluminum scandium nitride/2D channel ferroelectric field-effect-transistor memory. *Nano. Lett.* **2021**, *21*, 3753-61. DOI

9. Hu, Z.; Cho, H.; Rai, R. K.; et al. Demonstration of highly scaled AlScN ferroelectric diode memory with storage density > 100 Mbit/mm^2. *arXiv* **2025**, 2504.13283. DOI
10. Pradhan, D. K.; Moore, D. C.; Kim, G.; et al. A scalable ferroelectric non-volatile memory operating at 600 °C. *Nat. Electron.* **2024**, *7*, 348-55. DOI
11. Dai, X.; Hua, Q.; Jiang, C.; et al. Artificial synapse based on a tri-layer AlN/AlScN/AlN stacked memristor for neuromorphic computing. *Nano. Energy.* **2024**, *124*, 109473. DOI
12. Nomoto, K.; Casamento, J.; Nguyen, T. S.; et al. AlScN/GaN HEMTs with 4 A/mm on-current and maximum oscillation frequency >130 GHz. *Appl. Phys. Express.* **2025**, *18*, 016506. DOI
13. Zhao, C.; Xu, B.; Wang, Z.; Wang, Z. Boron-doped III-V semiconductors for Si-based optoelectronic devices. *J. Semicond.* **2020**, *41*, 011301. DOI
14. Cohen, A.; Li, J.; Cohen, H.; et al. Local environment of Sc and Y dopant ions in aluminum nitride thin films. *ACS. Appl. Electron. Mater.* **2024**, *6*, 853-61. DOI PubMed PMC
15. Anggraini, S. A.; Uehara, M.; Hirata, K.; Yamada, H.; Akiyama, M. Polarity inversion of aluminum nitride thin films by using Si and MgSi dopants. *Sci. Rep.* **2020**, *10*, 4369. DOI PubMed PMC
16. Alam, M. N.; Olszewski, O. Z.; Campanella, H.; Nolan, M. Large piezoelectric response and ferroelectricity in Li and V/Nb/Ta Co-doped w-AlN. *ACS. Appl. Mater. Interfaces.* **2021**, *13*, 944-54. DOI
17. Yokoyama, T.; Iwazaki, Y.; Onda, Y.; Nishihara, T.; Sasajima, Y.; Ueda, M. Highly piezoelectric co-doped AlN thin films for wideband FBAR applications. *IEEE. Trans. Ultrason. Ferroelectr. Freq. Control.* **2015**, *62*, 1007-15. DOI PubMed
18. Startt, J.; Quazi, M.; Sharma, P.; et al. Unlocking AlN piezoelectric performance with earth-abundant dopants. *Adv. Elect. Mater.* **2023**, *9*, 2201187. DOI
19. Savant, C.; Gund, V.; Nomoto, K.; et al. Ferroelectric AlBN films by molecular beam epitaxy. *Appl. Phys. Lett.* **2024**, *125*, 072902. DOI
20. Anggraini, S. A.; Uehara, M.; Yamada, H.; Akiyama, M. Investigating the piezoelectric response of Mg-Ti-doped-AlN thin films for sensor application. 2017 IEEE Sensors, Glasgow, UK, 29 October 2017 - 01 November 2017; pp. 1-3. DOI
21. Eliseev, E. A.; Morozovska, A. N.; Maria, J. P.; Chen, L. Q.; Gopalan, V. Thermodynamic theory of proximity ferroelectricity. *Phys. Rev. X.* **2025**, *15*, 021058. DOI
22. Stutzmann, M.; Ambacher, O.; Eickhoff, M.; et al. Playing with polarity. *Phys. Stat. Sol. B.* **2001**, *228*, 505-12. DOI
23. Calderon, S.; Hayden, J.; Baksa, S. M.; et al. Atomic-scale polarization switching in wurtzite ferroelectrics. *Science* **2023**, *380*, 1034-8. DOI
24. Maria, J. P.; Skidmore, C. Data for "Proximity ferroelectricity in wurtzite heterostructures". *Scholarsphere* **2024**,. DOI
25. Drury, D.; Yazawa, K.; Zakutayev, A.; Hanrahan, B.; Brennecka, G. High-temperature ferroelectric behavior of $Al_{0.7}Sc_{0.3}N$. *Micromachines* **2022**, *13*, 887. DOI PubMed PMC
26. Zhu, W.; Hayden, J.; He, F.; et al. Strongly temperature dependent ferroelectric switching in AlN, $Al_{1-x}Sc_xN$, and $Al_{1-x}B_xN$ thin films. *Appl. Phys. Lett.* **2021**, *119*, 062901. DOI
27. Höglund, C.; Birch, J.; Alling, B.; et al. Wurtzite structure $Sc_{1-x}Al_xN$ solid solution films grown by reactive magnetron sputter epitaxy: structural characterization and first-principles calculations. *J. Appl. Phys.* **2010**, *107*, 123515. DOI
28. Saha, B.; Saber, S.; Naik, G. V.; et al. Development of epitaxial $Al_{1-x}Sc_xN$ for artificially structured metal/semiconductor superlattice metamaterials: epitaxial $Al_xSc_{1-x}N$ for artificially structured superlattice metamaterials. *Phys. Status. Solidi. B.* **2015**, *252*, 251-9. DOI
29. Brien, V.; Pigeat, P. Correlation between the oxygen content and the morphology of AlN films grown by r.f. magnetron sputtering. *J. Crystal. Growth.* **2008**, *310*, 3890-5. DOI
30. Ye, K. H.; Han, G.; Yeu, I. W.; Hwang, C. S.; Choi, J. Atomistic understanding of the ferroelectric properties of a wurtzite-structure $(AlN)_n/(ScN)_m$ superlattice. *Phys. Rap. Res.* **2021**, *15*, 2100009. DOI
31. Dawber, M.; Chandra, P.; Littlewood, P. B.; Scott, J. F. Depolarization corrections to the coercive field in thin-film ferroelectrics. *J. Phys. Condens. Matter.* **2003**, *15*, L393-8. DOI
32. Hayden, J.; Hossain, M. D.; Xiong, Y.; et al. Ferroelectricity in boron-substituted aluminum nitride thin films. *Phys. Rev. Mater.* **2021**, *5*, 044412. DOI
33. Ferri, K.; Bachu, S.; Zhu, W.; et al. Ferroelectrics everywhere: ferroelectricity in magnesium substituted zinc oxide thin films. *J. App. Phys.* **2021**, *130*, 044101. DOI
34. Moriwake, H.; Yokoi, R.; Taguchi, A.; et al. A computational search for wurtzite-structured ferroelectrics with low coercive voltages. *APL. Mater.* **2020**, *8*, 121102. DOI
35. Dai, Y.; Wu, M. Covalent-like bondings and abnormal formation of ferroelectric structures in binary ionic salts. *Sci. Adv.* **2023**, *9*, eadf8706. DOI PubMed PMC
36. Scott, J. F. Applications of modern ferroelectrics. *Science* **2007**, *315*, 954-9. DOI PubMed
37. He, F.; Zhu, W.; Hayden, J.; et al. Frequency dependence of wake-up and fatigue characteristics in ferroelectric $Al_{0.93}B_{0.07}N$ thin films. *Acta. Mater.* **2024**, *266*, 119678. DOI
38. Zhu, W.; He, F.; Hayden, J.; et al. Wake-up in $Al_{1-x}B_xN$ ferroelectric films. *Adv. Electron. Mater.* **2022**, *8*, 2100931. DOI
39. Yazawa, K.; Hayden, J.; Maria, J. P.; et al. Anomalously abrupt switching of wurtzite-structured ferroelectrics: simultaneous non-linear nucleation and growth model. *Mater. Horiz.* **2023**, *10*, 2936-44. DOI
40. Momida, H.; Teshigahara, A.; Oguchi, T. Strong enhancement of piezoelectric constants in $Sc_xAl_{1-x}N$: first-principles calculations.

AIP. Adv. **2016**, *6*, 065006. DOI

41. Messi, F.; Patidar, J.; Rodkey, N.; Dräyer, C. W.; Trassin, M.; Siol, S. Ferroelectric AlScN thin films with enhanced polarization and low leakage enabled by high-power impulse magnetron sputtering. *APL. Mater.* **2025**, *13*, 051123. DOI
42. Sun, W.; Zhou, J.; Jin, F.; Liu, N.; Zheng, S.; Li, B. Temperature dependence in coercive field of ferroelectric AlScN integrated on Si substrate, In 2024 IEEE International Conference on IC Design and Technology (ICICDT). Singapore; 2024, pp. 1-4. DOI
43. Hornsteiner, J.; Born, E.; Fischerauer, G.; Riha, E. Surface acoustic wave sensors for high-temperature applications, In Proceedings of the 1998 IEEE International Frequency Control Symposium, 1998; pp. 615-20. DOI
44. Yazawa, K.; Drury, D.; Zakutayev, A.; Brennecka, G. L. Reduced coercive field in epitaxial thin film of ferroelectric wurtzite $Al_{0.7}Sc_{0.3}N$. *Appl. Phys. Lett.* **2021**, *118*, 162903. DOI
45. Tasnádi, F.; Alling, B.; Höglund, C.; et al. Origin of the anomalous piezoelectric response in wurtzite $Sc_xAl_{1-x}N$ alloys. *Phys. Rev. Lett.* **2010**, *104*, 137601. DOI
46. Fichtner, S.; Wolff, N.; Lofink, F.; Kienle, L.; Wagner, B. AlScN: a III-V semiconductor based ferroelectric. *J. Appl. Phys.* **2019**, *125*, 114103. DOI
47. Galsin, J. S. Chapter 1 - Crystal Structure of Solids. Solid State Physics. Elsevier; 2019. pp. 1-36. DOI
48. Liu, X.; Zheng, J.; Wang, D.; et al. Aluminum scandium nitride-based metal-ferroelectric-metal diode memory devices with high on/off ratios. *Appl. Phys. Lett.* **2021**, *118*, 202901. DOI
49. Wang, J.; Park, M.; Mertin, S.; Pensala, T.; Ayazi, F.; Ansari, A. A high-k_t^2 switchable ferroelectric $Al_{0.7}Sc_{0.3}N$ film bulk acoustic resonator. In 2020 Joint Conference of the IEEE International Frequency Control Symposium and International Symposium on Applications of Ferroelectrics (IFCS-ISAF), Keystone, CO, USA; 2020, pp. 1-3. DOI
50. Herrera, B.; Pirro, M.; Giribaldi, G.; Colombo, L.; Rinaldi, M. AlScN programmable ferroelectric micromachined ultrasonic transducer (FMUT). In 2021 21st International Conference on Solid-State Sensors, Actuators and Microsystems (Transducers), Orlando, FL, USA; 2021, pp. 38-41. DOI
51. Rassay, S.; Mo, D.; Li, C.; Choudhary, N.; Forgey, C.; Tabrizian, R. Intrinsically switchable ferroelectric scandium aluminum nitride lamb-mode resonators. *IEEE. Electron. Device. Lett.* **2021**, *42*, 1065-8. DOI
52. Zhang, S.; Holec, D.; Fu, W. Y.; Humphreys, C. J.; Moram, M. A. Tunable optoelectronic and ferroelectric properties in Sc-based III-nitrides. *J. App. Phys.* **2013**, *114*, 133510. DOI
53. Business Research Insights. Thin film piezoelectric devices market size, share, growth, trends and industry analysis, by type (AlN Thin Film, PZT Thin Film), by application (Consumer Electronics, Healthcare, Aerospace and Defense, Others), regional insights and forecast From 2025 to 2033 . Available from: https://www.businessresearchinsights.com/market-reports/thin-film-piezoelectric-devices-market-110756 [Last accessed on 28 Jul 2025].
54. Höglund, C.; Bareño, J.; Birch, J.; Alling, B.; Czigány, Z.; Hultman, L. Cubic $Sc_{1-x}Al_xN$ solid solution thin films deposited by reactive magnetron sputter epitaxy onto ScN(111). *J. Appl. Phys.* **2009**, *105*, 113517. DOI
55. dos Santos, R. B.; Rivelino, R.; de Brito Mota, F.; Gueorguiev, G. K.; Kakanakova-Georgieva, A. Dopant species with Al-Si and N-Si bonding in the MOCVD of AlN implementing trimethylaluminum, ammonia and silane. *J. Phys. D. Appl. Phys.* **2015**, *48*, 295104. DOI
56. Taniyasu, Y.; Kasu, M.; Makimoto, T. An aluminium nitride light-emitting diode with a wavelength of 210 nanometres. *Nature* **2006**, *441*, 325-8. DOI PubMed
57. Bernardini, F.; Fiorentini, V.; Vanderbilt, D. Spontaneous polarization and piezoelectric constants of III-V nitrides. *Phys. Rev. B.* **1997**, *56*, R10024-7. DOI
58. Aubert, T.; Bardong, J.; Legrani, O.; et al. *In situ* high-temperature characterization of AlN-based surface acoustic wave devices. *J. Appl. Phys.* **2013**, *114*, 014505. DOI
59. Aubert, T.; Elmazria, O.; Assouar, B.; Hamdan, A.; Genève, D. Reliability of AlN/Sapphire bilayer structure for high-temperature SAW applications. In 2010 IEEE International Ultrasonics Symposium, San Diego, CA, USA; 2010, pp. 1490-3. DOI
60. Akiyama, M.; Kamohara, T.; Kano, K.; Teshigahara, A.; Takeuchi, Y.; Kawahara, N. Enhancement of piezoelectric response in scandium aluminum nitride alloy thin films prepared by dual reactive cosputtering. *Adv. Mater.* **2009**, *21*, 593-6. DOI PubMed
61. Deng, R.; Jiang, K.; Gall, D. Optical phonon modes in $Al_{1-x}Sc_xN$. *J. Appl. Phys.* **2014**, *115*, 013506. DOI
62. Jin, E. N.; Hardy, M. T.; Mock, A. L.; et al. Band alignment of $Sc_xAl_{1-x}N$/GaN heterojunctions. *ACS. Appl. Mater. Interfaces.* **2020**, *12*, 52192-200. DOI
63. Constantin, C.; Brithen, H. A.; Haider, M. B.; Ingram, D.; Smith, A. R. ScGaN alloy growth by molecular beam epitaxy: evidence for a metastable layered hexagonal phase. *Phys. Rev. B.* **2004**, *70*, 239902. DOI
64. Moram, M. A.; Zhang, S. ScGaN and ScAlN: emerging nitride materials. *J. Mater. Chem. A.* **2014**, *2*, 6042-50. DOI
65. Tholander, C.; Birch, J.; Tasnádi, F.; et al. Ab initio calculations and experimental study of piezoelectric Y In1-N thin films deposited using reactive magnetron sputter epitaxy. *Acta. Mater.* **2016**, *105*, 199-206. DOI
66. Umeda, K.; Kawai, H.; Honda, A.; Akiyama, M.; Kato, T.; Fukura, T. Piezoelectric properties of ScAlN thin films for piezo-MEMS devices, In IEEE 26th International Conference on Micro Electro Mechanical Systems (MEMS), Taipei, Taiwan; 2013, pp. 733-6. DOI
67. Liauh, W. J.; Wu, S.; Huang, J. L.; Lii, D. F.; Lin, Z. X.; Yeh, W. K. Microstructure and piezoelectric properties of reactively sputtered highly C-axis $Sc_xAl_{1-x}N$ thin films on diamond-like carbon/Si substrate. *Surf. Coat. Technol.* **2016**, *308*, 101-7. DOI
68. Talley, K. R.; Millican, S. L.; Mangum, J.; et al. Implications of heterostructural alloying for enhanced piezoelectric performance of

(Al,Sc)N. *Phys. Rev. Mater.* **2018**, *2*, 063802. DOI

69. Furuta, K.; Hirata, K.; Anggraini, S. A.; Akiyama, M.; Uehara, M.; Yamada, H. First-principles calculations of spontaneous polarization in ScAlN. *J. Appl. Phys.* **2021**, *130*, 024104. DOI
70. Lu, H.; Schönweger, G.; Petraru, A.; Kohlstedt, H.; Fichtner, S.; Gruverman, A. Domain dynamics and resistive switching in ferroelectric $Al_{1-x}Sc_xN$ thin film capacitors. *Adv. Funct. Mater.* **2024**, *34*, 2315169. DOI
71. Tybell, T.; Paruch, P.; Giamarchi, T.; Triscone, J. M. Domain wall creep in epitaxial ferroelectric $Pb(Zr_{0.2}Ti_{0.08})O_3$ thin films. *Phys. Rev. Lett.* **2002**, *89*, 097601. DOI PubMed
72. Wang, D.; Wang, D.; Zhou, P.; et al. On the surface oxidation and band alignment of ferroelectric $Sc_{0.18}Al_{0.82}N$/GaN heterostructures. *Appl. Surf. Sci.* **2023**, *628*, 157337. DOI
73. Dreyer, C. E.; Janotti, A.; Van de Walle, C. G.; Vanderbilt, D. Correct implementation of polarization constants in Wurtzite materials and impact on III-nitrides. *Phys. Rev. X.* **2016**, *6*, 021038. DOI
74. Satoh, S.; Ohtaka, K.; Shimatsu, T.; Tanaka, S. Crystal structure deformation and phase transition of AlScN thin films in whole Sc concentration range. *J. Appl. Phys.* **2022**, *132*, 025103. DOI
75. Petrich, R.; Bartsch, H.; Tonisch, K.; Jaekel, K.; Barth, S.; Bartzsch, H. Investigation of ScAlN for piezoelectric and ferroelectric applications. In 2019 22nd European Microelectronics and Packaging Conference & Exhibition (EMPC), Pisa, Italy; 2019, pp. 1-5. DOI
76. Denton, A. R.; Ashcroft, N. W. Vegard's law. *Phys. Rev. A.* **1991**, *43*, 3161-4. DOI PubMed
77. Koh, Y. R.; Shi, J.; Wang, B.; et al. Thermal boundary conductance across epitaxial metal/sapphire interfaces. *Phys. Rev. B.* **2020**, *102*, 205304. DOI
78. Milyutin, E.; Harada, S.; Martin, D.; et al. Sputtering of (001)AlN thin films: control of polarity by a seed layer. *J. Vac. Sci. Technol. B.* **2010**, *28*, L61-3. DOI
79. Yasuoka, S.; Mizutani, R.; Ota, R.; et al. Tunable ferroelectric properties in Wurtzite $(Al_{0.8}Sc_{0.2})N$ via crystal anisotropy. *ACS. Appl. Electron. Mater.* **2022**, *4*, 5165-70. DOI
80. Farrer, N.; Bellaiche, L. Properties of hexagonal ScN versus wurtzite GaN and InN. *Phys. Rev. B.* **2002**, *66*, 201203. DOI
81. Yazawa, K.; Mangum, J. S.; Gorai, P.; Brennecka, G. L.; Zakutayev, A. Local chemical origin of ferroelectric behavior in wurtzite nitrides. *J. Mater. Chem. C.* **2022**, *10*, 17557-66. DOI
82. Murray, J. L. The Al-Sc (aluminum-scandium) system. *J. Phase. Equilib.* **1998**, *19*, 380-4. DOI
83. Moriarty, J. L.; Humphreys, J. E.; Gordon, R. O.; Baenziger, N. C. X-ray examination of some rare-earth-containing binary alloy systems. *Acta. Cryst.* **1966**, *21*, 840-1. DOI
84. Gschneidner, K. A.; Calderwood, F. W. The Alt-Sc (aluminum-scandium) system. *Bull. Alloy. Phase. Diagr.* **1989**, *10*, 34-6. DOI
85. Schob, O.; Parthé, E. *AB* compounds with Sc, Y and rare earth metals. I. Scandium and yttrium compounds with CrB and CsCl structure. *Acta. Cryst.* **1965**, *19*, 214-24. DOI
86. Eymond, S.; Parthé, E. Sc_2Al with Ni_2In structure type. *J. Less. Common. Metals.* **1969**, *19*, 441-3. DOI
87. Romano, L. T.; Northrup, J. E.; O'keefe, M. A. Inversion domains in GaN grown on sapphire. *Appl. Phys. Lett.* **1996**, *69*, 2394-6. DOI
88. Northrup, J. E.; Neugebauer, J.; Romano, L. T. Inversion domain and stacking mismatch boundaries in GaN. *Phys. Rev. Lett.* **1996**, *77*, 103-6. DOI
89. Dawber, M.; Bousquet, E. New developments in artificially layered ferroelectric oxide superlattices. *MRS. Bull.* **2013**, *38*, 1048-55. DOI
90. Badylevich, M.; Shamuilia, S.; Afanas'ev, V. V.; Stesmans, A.; Fedorenko, Y. G.; Zhao, C. Electronic structure of the interface of aluminum nitride with Si(100). *J. Appl. Phys.* **2008**, *104*, 093713. DOI
91. Wang, D.; Wang, P.; Mondal, S.; et al. Thickness scaling down to 5 nm of ferroelectric ScAlN on CMOS compatible molybdenum grown by molecular beam epitaxy. *Appl. Phys. Lett.* **2023**, *122*, 052101. DOI
92. Yasuoka, S.; Mizutani, R.; Ota, R.; et al. Enhancement of crystal anisotropy and ferroelectricity by decreasing thickness in (Al,Sc)N films. *J. Ceram. Soc. Japan.* **2022**, *130*, 436-41. DOI
93. Janovec, V. On the theory of the coercive field of single-domain crystals of $BaTiO_3$. *Czech. J. Phys.* **1958**, *8*, 3-15. DOI
94. Ke, C.; Hu, Y.; Liu, S. Depolarization induced III-V triatomic layers with tristable polarization states. *Nanoscale. Horiz.* **2023**, *8*, 616-23. DOI PubMed
95. Mizuno, T.; Umeda, K.; Aida, Y.; Honda, A.; Akiyama, M.; Nagase, T. Germanium aluminum nitride thin films for piezo-MEMS devices. In 2017 19th International Conference on Solid-State Sensors, Actuators and Microsystems (TRANSDUCERS), Kaohsiung, Taiwan; 2017, pp. 1891-4. DOI
96. Song, Y.; Perez, C.; Esteves, G.; et al. Thermal conductivity of aluminum scandium nitride for 5G mobile applications and beyond. *ACS. Appl. Mater. Interfaces.* **2021**, *13*, 19031-41. DOI
97. Tagantsev, A. K. Comment on "Ab initio study of the spontaneous polarization of pyroelectric BeO". *Phys. Rev. Lett.* **1992**, *69*, 389. DOI PubMed
98. Posternak, M.; Baldereschi, A.; Catellani, A.; Resta, R. Ab initio study of the spontaneous polarization of pyroelectric BeO. *Phys. Rev. Lett.* **1990**, *64*, 1777-80. DOI PubMed
99. Martin, R. M. Comment on calculations of electric polarization in crystals. *Phys. Rev. B.* **1974**, *9*, 1998-9. DOI
100. Resta, R. Theory of the electric polarization in crystals. *Ferroelectrics* **1992**, *136*, 51-5. DOI

101. Bernardini, F.; Fiorentini, V.; Vanderbilt, D. Accurate calculation of polarization-related quantities in semiconductors. *Phys. Rev. B.* **2001**, *63*, 193201. DOI
102. Yoo, S.; Todorova, M.; Neugebauer, J.; Van de Walle, C. G. Microscopic origin of polarization charges at GaN/(Al,Ga)N interfaces. *Phys. Rev. Appl.* **2023**, *19*, 064037. DOI
103. Strak, P.; Kempisty, P.; Sakowski, K.; et al. Polarization spontaneous and piezo: fundamentals and their implementation in ab initio calculations. *ArXiv* **2024**, 2407.01134. DOI
104. Uehara, M.; Mizutani, R.; Yasuoka, S.; et al. Lower ferroelectric coercive field of ScGaN with equivalent remanent polarization as ScAlN. *Appl. Phys. Express.* **2022**, *15*, 081003. DOI
105. Lee, C.; Din, N. U.; Yazawa, K.; Brennecka, G. L.; Zakutayev, A.; Gorai, P. Emerging materials and design principles for wurtzite-type ferroelectrics. *Matter* **2024**, *7*, 1644-59. DOI
106. Gall, D.; Städele, M.; Järrendahl, K.; et al. Electronic structure of ScN determined using optical spectroscopy, photoemission, and *ab initio* calculations. *Phys. Rev. B.* **2001**, *63*, 1251191-9. DOI
107. Gall, D.; Petrov, I.; Greene, J. E. Epitaxial $Sc_{1-x}Ti_xN(001)$: optical and electronic transport properties. *J. Appl. Phys.* **2001**, *89*, 401-9. DOI
108. Fiorentini, V.; Bernardini, F.; Ambacher, O. Evidence for nonlinear macroscopic polarization in III-V nitride alloy heterostructures. *Appl. Phys. Lett.* **2002**, *80*, 1204-6. DOI
109. Wu, J.; Walukiewicz, W.; Yu, K. M.; et al. Small band gap bowing in $In_{1-x}Ga_xN$ alloys. *Appl. Phys. Lett.* **2002**, *80*, 4741-3. DOI
110. Wolff, N.; Fichtner, S.; Haas, B.; et al. Atomic scale confirmation of ferroelectric polarization inversion in wurtzite-type AlScN. *J. Appl. Phys.* **2021**, *129*, 034103. DOI
111. Schönweger, G.; Petraru, A.; Islam, M. R.; et al. From fully strained to relaxed: epitaxial ferroelectric $Al_{1-x}Sc_xN$ for III-N technology. *Adv. Funct. Mater.* **2022**, *32*, 2109632. DOI
112. Uehara, M.; Mizutani, R.; Yasuoka, S.; et al. Demonstration of ferroelectricity in ScGaN thin film using sputtering method. *Appl. Phys. Lett.* **2021**, *119*, 172901. DOI
113. Wang, D.; Wang, P.; Wang, B.; Mi, Z. Fully epitaxial ferroelectric ScGaN grown on GaN by molecular beam epitaxy. *Appl. Phys. Lett.* **2021**, *119*, 111902. DOI
114. Wang, D.; Wang, P.; Mondal, S.; Xiao, Y.; Hu, M.; Mi, Z. Impact of dislocation density on the ferroelectric properties of ScAlN grown by molecular beam epitaxy. *Appl. Phys. Lett.* **2022**, *121*, 042108. DOI
115. Dinh, D. V.; Lähnemann, J.; Geelhaar, L.; Brandt, O. Lattice parameters of $Sc_xAl_{1-x}N$ layers grown on GaN(0001) by plasma-assisted molecular beam epitaxy. *Appl. Phys. Lett.* **2023**, *122*, 152103. DOI
116. Zhang, D.; Jin, L.; Li, J.; et al. MBE growth of ultra-thin GeSn film with high Sn content and its infrared/terahertz properties. *J. Alloys. Compd.* **2016**, *665*, 131-6. DOI
117. Zeng, Y.; Lei, Y.; Wang, Y.; et al. High quality epitaxial piezoelectric and ferroelectric Wurtzite $Al_{1-x}Sc_xN$ thin films. *Small. Methods.* **2025**, *9*, e2400722. DOI
118. Tang, M.; Dai, L.; Cheng, M.; et al. High-throughput screening thickness-dependent resistive switching in $SrTiO_3$ thin films for robust electronic synapse. *Adv. Funct. Mater.* **2023**, *33*, 2213874. DOI
119. Yang, Y.; Li, X.; Zhou, D.; et al. Effects of temperature on PO and resistivity of ScAlN film. *Surf. Eng.* **2015**, *31*, 775-8. DOI
120. Zukauskaite, A.; Wingqvist, G.; Palisaitis, J.; et al. Microstructure and dielectric properties of piezoelectric magnetron sputtered w-$Sc_xAl_{1-x}N$ thin films. *J. Appl. Phys.* **2012**, *111*, 093527. DOI
121. Pérez-Campos, A.; Sinusía, L. M.; Garcia-Garcia, F. J.; Chen, Z.; Iriarte, G. F. Synthesis of ScAlN thin films on Si (100) substrates at room temperature. *Microsyst. Technol.* **2018**, *24*, 2711-8. DOI
122. van der Wel, B. Y.; van der Zouw, K.; Aarnink, A. A. I.; Kovalgin, A. Y. Area-Selective low-pressure thermal atomic layer deposition of aluminum nitride. *J. Phys. Chem. C.* **2023**, *127*, 17134-45. DOI
123. Bartram, M. E.; Michalske, T. A.; Rogers, J. W.; Paine, R. T. Nucleation and growth of aluminum nitride: self-limiting reactions and the regeneration of active sites using sequential exposures of trimethylaluminum and ammonia on silica at 600 K. *Chem. Mater.* **1993**, *5*, 1424-30. DOI
124. Detavernier, C.; Dendooven, J.; Deduytsche, D.; Musschoot, J. Thermal versus plasma-enhanced ALD: growth kinetics and conformality. *ECS. Trans.* **2008**, *16*, 239. DOI
125. Bui, H. V.; Nguyen, M. D.; Wiggers, F. B.; Aarnink, A. A. I.; de Jong, M. P.; Kovalgin, A. Y. Self-limiting growth and thickness- and temperature- dependence of optical constants of ALD AlN thin films. *ECS. J. Solid. State. Sci. Technol.* **2014**, *3*, 101-6. DOI
126. Seppänen, H.; Kim, I.; Etula, J.; Ubyivovk, E.; Bouravleuv, A.; Lipsanen, H. Aluminum nitride transition layer for power electronics applications grown by plasma-enhanced atomic layer deposition. *Materials* **2019**, *12*, 406. DOI PubMed PMC
127. Schilirò, E.; Giannazzo, F.; Di, F. S.; et al. Highly homogeneous current transport in ultra-thin aluminum nitride (AlN) epitaxial films on gallium nitride (GaN) deposited by plasma enhanced atomic layer deposition. *Nanomaterials* **2021**, *11*, 3316. DOI PubMed PMC
128. Samii, R.; Zanders, D.; Buttera, S. C.; et al. Synthesis and thermal study of hexacoordinated Aluminum(III) triazenides for use in atomic layer deposition. *Inorg. Chem.* **2021**, *60*, 4578-87. DOI PubMed PMC
129. Rouf, P.; Samii, R.; Rönnby, K.; et al. Hexacoordinated Gallium(III) triazenide precursor for epitaxial gallium nitride by atomic layer deposition. *Chem. Mater.* **2021**, *33*, 3266-75. DOI
130. Pedersen, H.; Hsu, C. W.; Nepal, N.; Woodward, J. M.; Eddy, C. R. J. Atomic layer deposition as the enabler for the metastable

semiconductor InN and its alloys. *Cryst. Growth. Des.* **2023**, *23*, 7010-25. DOI PubMed PMC

131. Seppänen, H.; Prozheev, I.; Kauppinen, C.; Suihkonen, S.; Mizohata, K.; Lipsanen, H. Effect of atomic layer annealing in plasma-enhanced atomic layer deposition of aluminum nitride on silicon. *J. Vac. Sci. Technol. A.* **2023**, *41*, 052401. DOI
132. Shih, H. Y.; Lee, W. H.; Kao, W. C.; et al. Low-temperature atomic layer epitaxy of AlN ultrathin films by layer-by-layer, in-situ atomic layer annealing. *Sci. Rep.* **2017**, *7*, 39717. DOI PubMed PMC
133. Kao, W.; Jhong, F.; Yin, Y.; Lin, H.; Chen, M. High-quality AlN epilayers prepared by atomic layer deposition and large-area rapid electron beam annealing. *Mater. Chem. Phys.* **2023**, *304*, 127895. DOI
134. Available from: https://www.atomiclimits.com/alddatabase/ [Last accessed on 28 Jul 2025].
135. Nepal, N.; Anderson, V. R.; Hite, J. K.; Eddy, C. R. Growth and characterization of III-N ternary thin films by plasma assisted atomic layer epitaxy at low temperatures. *Thin. Solid. Films.* **2015**, *589*, 47-51. DOI
136. Tian, L.; Ponton, S.; Benz, M.; et al. Aluminum nitride thin films deposited by hydrogen plasma enhanced and thermal atomic layer deposition. *Surf. Coat. Technol.* **2018**, *347*, 181-90. DOI
137. Ozgit, C.; Donmez, I.; Alevli, M.; Biyikli, N. Self-limiting low-temperature growth of crystalline AlN thin films by plasma-enhanced atomic layer deposition. *Thin. Solid. Films.* **2012**, *520*, 2750-5. DOI
138. Kot, M.; Henkel, K.; Naumann, F.; et al. Comparison of plasma-enhanced atomic layer deposition AlN films prepared with different plasma sources. *J. Vac. Sci. Technol. A.* **2019**, *37*, 020913. DOI
139. Ligl, J.; Leone, S.; Manz, C.; et al. Metalorganic chemical vapor phase deposition of AlScN/GaN heterostructures. *J. Appl. Phys.* **2020**, *127*, 195704. DOI
140. Frei, K.; Trejo-Hernández, R.; Schütt, S.; et al. Investigation of growth parameters for ScAlN-barrier HEMT structures by plasma-assisted MBE. *Jpn. J. Appl. Phys.* **2019**, *58*, SC1045. DOI
141. Wang, D.; Zheng, J.; Musavigharavi, P.; Zhu, W.; Foucher, A. C.; McKinstry, S. E. T. Ferroelectric switching in sub-20 nm aluminum scandium nitride thin films. *IEEE. Electron. Device. Lett.* **2020**, *41*, 1774-7. DOI
142. Kataoka, J.; Tsai, S.; Hoshii, T.; Wakabayashi, H.; Tsutsui, K.; Kakushima, K. A possible origin of the large leakage current in ferroelectric $Al_{1-x}Sc_xN$ films. *Jpn. J. Appl. Phys.* **2021**, *60*, 030907. DOI
143. Chen, S.; Tsai, S.; Mizutani, K.; et al. GaN high electron mobility transistors (HEMTs) with self-upward-polarized AlScN gate dielectrics toward enhancement-mode operation. *Jpn. J. Appl. Phys.* **2022**, *61*, SH1007. DOI
144. Ryoo, S. K.; Kim, K. D.; Park, H. W.; et al. Investigation of optimum deposition conditions of radio frequency reactive magnetron sputtering of $Al_{0.7}Sc_{0.3}N$ film with thickness down to 20 nm. *Adv. Electron. Mater.* **2022**, *8*, 2200726. DOI
145. Wang, P.; Wang, D.; Vu, N. M.; Chiang, T.; Heron, J. T.; Mi, Z. Fully epitaxial ferroelectric ScAlN grown by molecular beam epitaxy. *Appl. Phys. Lett.* **2021**, *118*, 223504. DOI
146. Liu, Z.; Luo, B.; Hou, B. Coexistence of ferroelectricity and ferromagnetism in Ni-doped $Al_{0.7}Sc_{0.3}N$ thin films. *Appl. Phys. Lett.* **2022**, *120*, 252904. DOI
147. Hardy, M. T.; Downey, B. P.; Nepal, N.; Storm, D. F.; Katzer, D. S.; Meyer, D. J. Epitaxial ScAlN grown by molecular beam epitaxy on GaN and SiC substrates. *Appl. Phys. Lett.* **2017**, *110*, 162104. DOI
148. Hardy, M. T.; Jin, E. N.; Nepal, N.; et al. Control of phase purity in high scandium fraction heteroepitaxial ScAlN grown by molecular beam epitaxy. *Appl. Phys. Express.* **2020**, *13*, 065509. DOI
149. Sandu, C. S.; Parsapour, F.; Mertin, S.; et al. Abnormal grain growth in AlScN thin films induced by complexion formation at crystallite interfaces. *Phys. Status. Solid.* **2019**, *216*, 1800569. DOI
150. Wang, J.; Park, M.; Mertin, S.; Pensala, T.; Ayazi, F.; Ansari, A. A film bulk acoustic resonator based on ferroelectric aluminum scandium nitride films. *J. Microelectromech. Syst.* **2020**, *29*, 741-7. DOI
151. Kreutzer, T. N.; Fichtner, S.; Wagner, B.; Lofink, F. A double-layer MEMS actuator based on ferroelectric polarization inversion in AlScN. In 2021 IEEE International Symposium on Applications of Ferroelectrics(ISAF), Sydney, Australia; 2021, pp. 1-3. DOI